Chapter 13
Outdoor Examples

In this final chapter, we illustrate different steps of the procedure of modelling from time series in more detail. For that, we use examples from the fields of electronics (Sect. 13.1), physiology (Sect. 13.2) and climatology (Sect. 13.3). They are presented in the order of decreasing amount of a priori information about an object: an appropriate model structure is completely known and only model parameters are estimated from data (Sect. 13.1); an appropriate model structure is partly known (Sect. 13.2); no specific ideas about suitable model equations are available (Sect. 13.3). For the sake of unity, we formulate the same purpose of empirical modelling in all the three cases, namely identification of directional couplings between the processes under study. This task has also been considered in the previous chapter, where a compact and more technical description of several techniques and applications has been given.

13.1 Coupled Electronic Generators

13.1.1 Object Description

An experimental object is a system of two self-sustained generators (Fig. 13.1) similar to that described in Dmitriev and Kislov (1989); Dmitriev et al. (1996). Both generators are constructed according to the same scheme and contain an *RC* low-pass filter (an element 1 in Fig. 13.1a), an *RLC* filter (an oscillatory circuit 2) and a non-linear element (an element 3) connected in a ring (Ponomarenko et al., 2004). The non-linear element with a quadratic transfer characteristic $U_{\text{out}} = A - B \cdot U_{\text{in}}^2$ consists of an electronic multiplier, which performs the operation of taking a squared value, and a summing amplifier, which adds the parameter A with a necessary sign to an output signal of the multiplier (Fig. 13.1b). Here, U_{out} is a voltage at the output of the non-linear element, B is a dimensional coefficient whose value is determined by the parameters of the electronic multiplier. A is used as a governing parameter. Under variations in A, one observes a transition to chaos via the cascade of period-doubling bifurcations in each generator.

B.P. Bezruchko, D.A. Smirnov, *Extracting Knowledge From Time Series*, Springer Series in Synergetics, DOI 10.1007/978-3-642-12601-7_13,

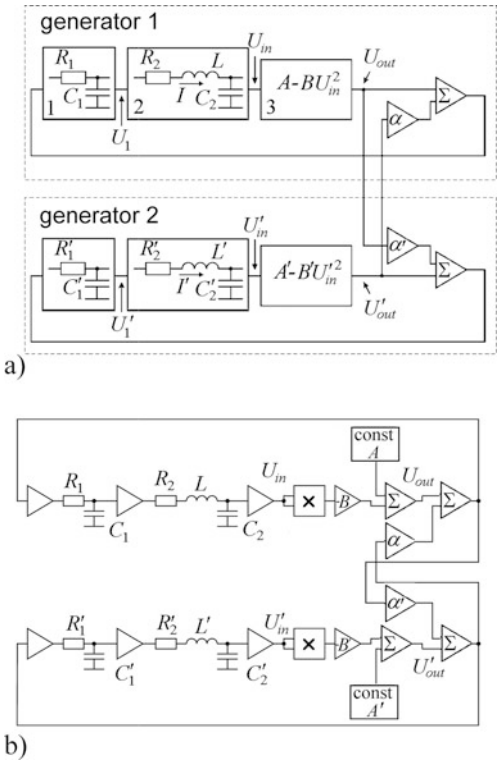

Fig. 13.1 Experimental set-up: (**a**) a more vivid block scheme; (**b**) a more detailed version. The parameters are $R_1 = 1000\,\Omega$, $R_2 = 60\,\Omega$, $C_1 = C_2 = 0.022\,\mu\text{F}$, $L = 6\,\text{mH}$, $B = 0.2\,\text{V}^{-1}$. Parameters of the generator 2 are the same up to an error of about 10%. A and A' control non-linear transfer functions of the non-linear elements, α and α' are coupling coefficients and Σ are summing amplifiers

Further, we denote the quantities relating to the second generator by a prime, while those for the first generator are not supplied with a prime. Interaction between the generators is possible due to the summing amplifiers Σ and the amplifiers with controlled gain factors α and α'. The latter ones serve to set the "interaction strength". By specifying different values of α and α', one provides bidirectional, unidirectional or zero coupling between the generators. Below, we describe the cases of uncoupled generators ($\alpha = \alpha' = 0$) and unidirectional coupling $2 \to 1$ ($\alpha \neq 0, \alpha' = 0$) for different values of A and A'. The settings considered are summarised in Table 13.1, where the corresponding dynamical regimes are identified as described below.

In what follows, the values of the parameters (such as inductance, capacity, resistance) in both generators are not regarded as a priori known. Only the equivalent electric scheme of Fig. 13.1 is considered as a priori known. Coupling character is revealed from data only with the use of the latter information.

Table 13.1 Parameters values and corresponding dynamical regimes considered. T is a characteristic timescale of the autonomous self-sustained oscillations (it is about 0.08 ms as described in Sect. 13.1.2). Namely, T corresponds to the highest peak in the power spectrum

Trial no.	Parameters				Dynamical regimes (Ponomarenko et al., 2004)
	A, V	A', V	α	α'	
1	4.8	3.8	0	0	Cycle of the period $1T$
2	4.8	3.8	0.05	0	Torus in the generator 1, cycle of the period $1T$ in the generator 2
3	4.8	3.8	0.9	0	Cycle of the period $2T$ in the generator 1, cycle of the period $1T$ in the generator 2
4	4.8	5.8	0.1	0	Chaos in both generators
5	4.8	5.8	0	0	Cycle of the period $1T$ in the generator 1, chaos in the generator 2
6	8.8	7.4	0	0	Chaos in both generators
7	8.8	7.4	0.1	0	Chaos in both generators

13.1.2 Data Acquisition and Preliminary Processing

Observed quantities x and x' are linearly dependent on the voltages U_{in} and U'_{in} : $x = a + U_{\text{in}}/b$ and $x' = a' + U'_{\text{in}}/b'$. The shift and scaling parameters a, b, a', b' are some constants adjusted so as to provide a maximally efficient usage of the dynamics range of a 12-bit analogue-to-digital converter exploited for the measurements. The values of a, b, a', b' are not measured, since it would complicate the experimental set-up. The sampling frequency is 1.2 MHz which corresponds approximately to 100 data points per characteristic oscillation period.

Time series of x and x' is shown in Fig. 13.2a, b for the case of unidirectional coupling $2 \rightarrow 1$ (Table 13.1, trial 4). The driving generator 2 exhibits a chaotic regime (see below). The generator 1 without coupling would demonstrate a periodic regime. The quantities x and x' are presented in arbitrary units. Namely, the raw numerical values at the output of the ADC are integers and cover the range approximately from -2000 to 2000. For the sake of convenience, we divide them by 1000 and get the signals x and x' with the oscillation amplitudes of the order of 1. A rationale behind such scaling is that making typical values of all the analysed quantities of the order of unity allows the reduction of the computational errors (induced by the truncation) during the model fitting.

Estimates of the power spectra (Sect. 6.4.2) and the autocorrelation functions (Sect. 4.1.2) are shown in Fig. 13.2c–h. The highest peak is observed at the frequency of 12.36 kHz for the generator 2 (Fig. 13.2d). It corresponds to the timescale of 0.08 ms (about 100 data points), which is the distance between successive maxima in Fig. 13.2b. The peak is quite well pronounced, but it is somewhat wider than that for a quasi-periodic regime shown in Fig. 6.14b and, especially, for a periodic regime in Fig. 6.14a. Additional peaks are seen at 6.2 kHz (the first subharmonic, which is manifested as the alternation of higher and lower maxima in Fig. 13.2b), 18.6, 24.7, 30.9 and 37.1 kHz (overtones induced by the non-linearity of the

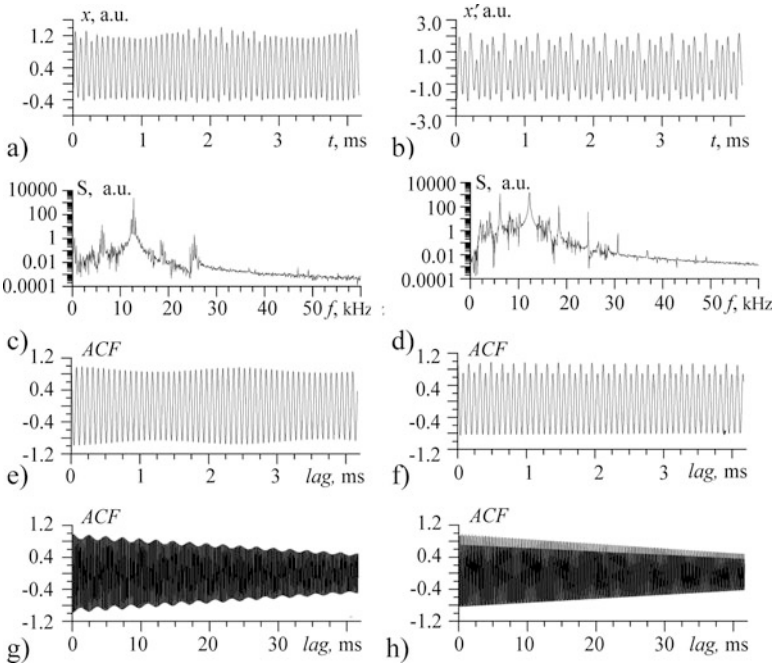

Fig. 13.2 Time series and their basic characteristics (Table 13.1, trial 4): the left column is for the generator 1; the right column is for the generator 2. Observed time series are shown in the panels (**a**) and (**b**), their periodograms in (**c**) and (**d**); their autocorrelation functions in (**e**) and (**f**) and, at different timescale, in (**g**) and (**h**). Both ACFs and periodograms are estimated from signals of length of 10^5 data points, rather than from the short pieces consisting of 5000 data points shown in the panels (**a**) and (**b**)

system and manifested as deviations of the temporal profile from a sinusoidal wave). The corresponding ACF exhibits a strong periodic component with a characteristic period of 0.08 ms and its subharmonic with a period twice as large. The ACF decreases with the time lag (Fig. 13.2h), but the rate of its decay is low: a linear envelope of the ACF reveals that the autocorrelations decrease from 1 to 0.5 over 40 ms (500 characteristic periods).

Projections of the orbits onto the plane of time-delayed coordinates are given in Fig. 13.3a, b. From Fig. 13.3b one can suspect a complex structure similar to a projection of a chaotic attractor e.g., like in Fig. 6.15. The regime observed in the generator 2 is, indeed, identified as chaotic, since we have evidenced its birth by tracing the evolution of the phase orbit of the generator under the parameter change (Ponomarenko et al., 2004). The regime under consideration has been established after a cascade of period-doubling bifurcations. We do not go into further details of the dynamical regime identification, since detection of chaos, estimation of fractal dimensions and similar questions are redundant for the formulated purpose of the model construction and the coupling estimation. In this example, a model dimension and even a complete structure of model equations are specified from physical considerations as presented below.

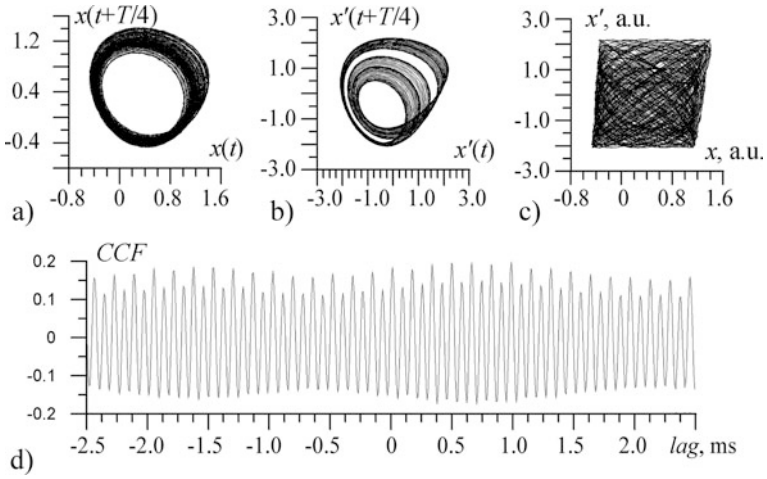

Fig. 13.3 Additional characteristics of the dynamics illustrated in Fig. 13.2: projections of the data onto different planes are shown in the panels (**a**), (**b**) and (**c**); cross-correlation function between $x(t)$ and $x'(t)$ is shown in panel (**d**)

The power spectrum and the ACF for the generator 1 are shown in Fig. 13.2c, e, g. A clear peak is observed at the frequency of 12.72 kHz (a natural frequency of the periodic oscillations in the generator 1). The satellite peaks observed at the close frequencies of 12.36 and 13.08 kHz are induced by the influence $2 \rightarrow 1$ and manifested as a periodic component of the ACF envelope with a period corresponding to the frequency mismatch of 0.36 kHz. The peaks at 6.2, 18.6 and 24.7 kHz are also seen in Fig. 13.2c. The ACF would not decrease for the non-driven generator 1; it decreases here due to the influence of the chaotic generator 2.

Traditional characteristics of the interdependence between the signals $x(t)$ and $x'(t)$ are illustrated in Fig. 13.3c, d. Figure 13.3c shows that a projection of the data onto the plane (x, x') fills almost a rectangular region. It means that even if the interdependence is present, it is not strong. This is confirmed by the cross-correlation function (Sect. 6.4.5) which takes absolute values less than 0.2, rather than close to 1, as illustrated in Fig. 13.3d.

13.1.3 Selection of the Model Equation Structure

Let us consider a single generator in the case of zero couplings. From Kirchhoff's laws, one can write down the following set of three ordinary first-order differential equations to model variations in currents and voltages:

$$\begin{aligned} C_1\,\mathrm{d}U_1/\mathrm{d}t &= (U_{\text{out}} - U_1)/R_1, \\ C_2\,\mathrm{d}U_{\text{in}}/\mathrm{d}t &= I, \\ L\,\mathrm{d}I/\mathrm{d}t &= U_1 - U_{\text{in}} - R_2 I. \end{aligned} \tag{13.1}$$

All the variables entering the model are indicated in Fig. 13.1. Since only the values of U_{in} are observed experimentally, it is desirable to rewrite the equations in terms of this quantity and its derivatives. Thereby, one avoids coping with hidden variables, which is often a difficult task (Sect. 8.2). Via some algebraic manipulations, equation (13.1) can be equivalently rewritten as

$$\frac{\mathrm{d}^3 U_{\text{in}}}{\mathrm{d}t^3} = -\left(\frac{1}{R_1 C_1} + \frac{R_2}{L}\right)\frac{\mathrm{d}^2 U_{\text{in}}}{\mathrm{d}t^2} - \frac{1}{LC_2}\left(1 + \frac{R_2 C_2}{R_1 C_1}\right)\frac{\mathrm{d}U_{\text{in}}}{\mathrm{d}t} + \frac{A - U_{\text{in}} - BU_{\text{in}}^2}{LC_2 R_1 C_1}. \tag{13.2}$$

For two generators, one gets the set of six first-order equations:

$$\begin{aligned}
&C_1\frac{\mathrm{d}U_1}{\mathrm{d}t} = \left(U_{\text{out}} - U_1 - \alpha U'_{\text{out}}\right)/R_1, && C'_1\frac{\mathrm{d}U'_1}{\mathrm{d}t} = \left(U'_{\text{out}} - U'_1 - \alpha' U_{\text{out}}\right)/R'_1,\\
&C_2\frac{\mathrm{d}U_{\text{in}}}{\mathrm{d}t} = I, && C'_2\frac{\mathrm{d}U'_{\text{in}}}{\mathrm{d}t} = I',\\
&L\frac{\mathrm{d}I}{\mathrm{d}t} = U_1 - U_{\text{in}} - R_2 I, && L'\frac{\mathrm{d}I'}{\mathrm{d}t} = U'_1 - U'_{\text{in}} - R'_2 I',
\end{aligned} \tag{13.3}$$

where the terms $\alpha U'_{\text{out}}$ and $\alpha' U_{\text{out}}$ describe the couplings between the generators. The equations can be rewritten in terms of the variables U_{in}, U'_{in} as

$$\begin{aligned}
\frac{\mathrm{d}^3 U_{\text{in}}}{\mathrm{d}t^3} &= -\left(\frac{1}{R_1 C_1} + \frac{R_2}{L}\right)\frac{\mathrm{d}^2 U_{\text{in}}}{\mathrm{d}t^2} - \frac{1}{LC_2}\left(1 + \frac{R_2 C_2}{R_1 C_1}\right)\frac{\mathrm{d}U_{\text{in}}}{\mathrm{d}t}\\
&\quad + \frac{A - U_{\text{in}} - BU_{\text{in}}^2}{LC_2 R_1 C_1} + \frac{\alpha\left(A' - B' U_{\text{in}}'^2\right)}{LC_2 R_1 C_1},\\
\frac{\mathrm{d}^3 U'_{\text{in}}}{\mathrm{d}t^3} &= -\left(\frac{1}{R'_1 C'_1} + \frac{R'_2}{L'}\right)\frac{\mathrm{d}^2 U'_{\text{in}}}{\mathrm{d}t^2} - \frac{1}{L'C'_2}\left(1 + \frac{R'_2 C'_2}{R'_1 C'_1}\right)\frac{\mathrm{d}U'_{\text{in}}}{\mathrm{d}t}\\
&\quad + \frac{A' - U'_{\text{in}} - B' U'^2_{\text{in}}}{L'C'_2 R'_1 C'_1} + \frac{\alpha'\left(A - BU_{\text{in}}^2\right)}{L'C'_2 R'_1 C'_1}.
\end{aligned} \tag{13.4}$$

To estimate model parameters from a time series of $x(t)$ and $x'(t)$, we specify the model structure as

$$\frac{\mathrm{d}^3 x}{\mathrm{d}t^3} = c_1\frac{\mathrm{d}^2 x}{\mathrm{d}t^2} + c_2\frac{\mathrm{d}x}{\mathrm{d}t} + c_3 + c_4 x + c_5 x^2 + c_6 x' + c_7 x'^2, \tag{13.5}$$

$$\frac{\mathrm{d}^3 x'}{\mathrm{d}t^3} = c'_1\frac{\mathrm{d}^2 x'}{\mathrm{d}t^2} + c'_2\frac{\mathrm{d}x'}{\mathrm{d}t} + c'_3 + c'_4 x' + c'_5 x'^2 + c'_6 x + c'_7 x^2, \tag{13.6}$$

where the terms $c_6 x'$, $c'_6 x$ absent from equation (13.4) are introduced to allow for the scaling and shift parameters a, b, a', b' in the measurement procedure. The unknown values of a, b, a', b' are not important, since they affect only the numerical values of the model coefficients c_k, c'_k, rather than model behaviour and relative

approximation error considered below. One can infer the presence of the influence $2 \rightarrow 1$ and $1 \rightarrow 2$ by comparing the models (13.5) and (13.6) with the models which do not allow for the coupling terms and read as

$$\frac{\mathrm{d}^3 x}{\mathrm{d}t^3} = c_1 \frac{\mathrm{d}^2 x}{\mathrm{d}t^2} + c_2 \frac{\mathrm{d}x}{\mathrm{d}t} + c_3 + c_4 x + c_5 x^2 \tag{13.7}$$

and

$$\frac{\mathrm{d}^3 x'}{\mathrm{d}t^3} = c'_1 \frac{\mathrm{d}^2 x'}{\mathrm{d}t^2} + c'_2 \frac{\mathrm{d}x'}{\mathrm{d}t} + c'_3 + c'_4 x' + c'_5 x'^2. \tag{13.8}$$

More precisely, we use two model-based approaches to reveal couplings. Firstly, we compare approximation errors for the individual models (13.7) or (13.8) to the errors for the joint models (13.5) or (13.6), respectively. This is similar to the characterisation of the Granger causality (Sect. 12.1). Secondly, we use a criterion which unites the analysis of couplings with the model validation and can be called a "free-run version" of the Granger causality. Namely, if an empirical model of the form (13.7) cannot reproduce the observed dynamics of x, while a model of the form (13.5) can do it, then one infers the presence of the influence $2 \rightarrow 1$ and its considerable effect on the dynamics. If already the model (13.5) describes the dynamics of x satisfactorily and the model (13.7) does not improve anything, then the influence $2 \rightarrow 1$ is insignificant. A similar comparison of the models (13.8) and (13.6) applies to the detection of the influence $1 \rightarrow 2$. If even the models (13.5) and (13.6) cannot adequately describe the observed dynamics, then the physical ideas behind the model equations are invalid and one must seek for other model structures.

13.1.4 Model Fitting, Validation and Usage

13.1.4.1 Individual Models

Let us start with the modelling of the generator 2 with the aid of the "individual" equation (13.8). We use the chaotic time series $x'(t)$ shown in Fig. 13.2b as a training time series. It is of a moderate length: $N = 5000$ data points, i.e. about 50 basic periods. The model (13.8) should be appropriate, since the generator 2 is not influenced by the generator 1. However, a complete validity of the model structure is not trivial, since the basic equation (13.2) is derived under the assumptions of strictly quadratic non-linearity (though the transfer characteristic follows a quadratic parabola with errors of about 1%), a constant inductance L (though it is realised with a ferrite core so that nonlinear properties might be observed at big oscillation amplitudes), etc.

According to the procedure described in the beginning of Chap. 8 and in Sect. 9.1, one first performs numerical differentiation of the signal $x'(t)$ to get the estimates

$$\frac{\mathrm{d}\hat{x}'}{\mathrm{d}t}, \frac{\mathrm{d}^2\hat{x}'}{\mathrm{d}t^2}, \frac{\mathrm{d}^3\hat{x}'}{\mathrm{d}t^3}$$

of the derivatives

$$\frac{\mathrm{d}x'}{\mathrm{d}t}, \frac{\mathrm{d}^2x'}{\mathrm{d}t^2}, \frac{\mathrm{d}^3x'}{\mathrm{d}t^3}$$

entering the model equation (13.8). We use a digital smoothing polynomial (Sect. 7.4.2): the estimates

$$\frac{\mathrm{d}\hat{x}'(t_n)}{\mathrm{d}t}, \frac{\mathrm{d}^2\hat{x}'(t_n)}{\mathrm{d}t^2}, \frac{\mathrm{d}^3\hat{x}'(t_n)}{\mathrm{d}t^3}$$

and a smoothed signal $\hat{x}'(t_n)$ at a time instant t_n are obtained from an algebraic polynomial of an order L fitted to the time window $\{t_n - m\Delta t; t_n + m\Delta t\}$ consisting of $2m+1$ data points. Let us note the following purely technical detail. For the sake of convenience, we rescale the time units similar to the above scaling of the variables x and x': the time units are selected so as to provide the values of the derivatives of the order of 1. This is achieved if the angular frequency of the oscillations becomes of the order of 1. Thus, we define the time units so that the sampling interval (which equals $1/1.2$ μs in the physical units) gets equal to $\Delta t = 0.1$.

Secondly, the model coefficients are estimated via minimisation of the error

$$\varepsilon^2 = \frac{1}{N-2m} \sum_{i=m+1}^{N-m} \left[\frac{\mathrm{d}^3\hat{x}'(t_i)}{\mathrm{d}t^3} - c'_1 \frac{\mathrm{d}^2\hat{x}'(t_i)}{\mathrm{d}t^2} - c'_2 \frac{\mathrm{d}\hat{x}'(t_i)}{\mathrm{d}t} - c'_3 - c'_4\hat{x}'(t_i) - c'_5\hat{x}'^2(t_i) \right]^2$$

The minimal relative approximation error is

$$\varepsilon_{\mathrm{rel}} = \sqrt{\min_{\{c'_k\}} \varepsilon^2 \Big/ \mathrm{var}[\mathrm{d}^3\hat{x}'/\mathrm{d}t^3]},$$

where "var" stands for the sample variance (Sect. 2.2.1) of the argument. Next, a free-run behaviour of an obtained model is simulated. A projection of a model phase orbit onto the plane $(x', \mathrm{d}x'/\mathrm{d}t)$ is compared to the corresponding projection of an observed data. For quantitative comparison, we compute a prediction time, i.e. a time interval τ_{pred}, over which the prediction error $\sigma(\tau) = \sqrt{\left\langle \left(x'(t_0+\tau) - x'_{\mathrm{pred}}(t_0+\tau)\right)^2 \right\rangle_{t_0}}$ (Sect. 2.2.4) rises up to $0.05\sqrt{\mathrm{var}[x']}$. Here, $x'_{\mathrm{pred}}(t_0+\tau)$ is a prediction at a time instant $t_0+\tau$ obtained by simulation of a model orbit from the initial condition $\hat{x}'(t_0)$, $\mathrm{d}\hat{x}'(t_0)/\mathrm{d}t$, $\mathrm{d}^2\hat{x}'(t_0)/\mathrm{d}t^2$ at the initial time instant t_0. A test time series of the length of 10000 data points (which is a continuation of the data segment shown in Fig. 13.2b) is used both for the qualitative comparison and for the prediction time estimation.

Table 13.2 Characteristics of the models (13.8) for different m and L

m	L	$\hat{c}'_1$	$\hat{c}'_2$	$\hat{c}'_3$	$\hat{c}'_4$	$\hat{c}'_5$	ε_{rel}	τ_{pred}
2	3	−15.9	−1.71	−2.20	−6.09	1.09	0.45	$0.05T$
5	3	−0.40	−0.44	−0.19	−0.15	0.12	0.78	$0.25T$
12	3	−0.42	−0.42	−0.17	−0.15	0.10	0.07	$0.25T$
40	3	−0.30	−0.20	−0.04	−0.05	0.03	0.11	$0.07T$
40	7	−0.43	−0.42	−0.18	−0.17	0.11	0.03	$0.71T$

We try different values of the parameters $L \geq 3$ and $m \geq L/2$. Model quality essentially depends on m and L, since these parameters determine the errors in the derivative estimates and, hence, the errors in the estimates of the model coefficients. The model coefficients and some characteristics are shown in Table 13.2. Thus, small values of m are not sufficient to reduce the noise influence so that the derivative estimates are very noisy as seen in Fig. 13.4 for $m = 2$ and $L = 3$. Both the second and the third derivatives are strongly noise corrupted. The corresponding model is completely invalid (Fig. 13.5); it exhibits a stable fixed point instead of chaotic oscillations (Fig. 13.5b, c), a very large approximation error $\varepsilon_{\text{rel}} = 0.45$ and a small prediction time $\tau_{\text{pred}} = 0.05T$, where the characteristic period is $T \approx 100\Delta t$ (Fig. 13.5a, d). Greater values of m at fixed $L = 3$ allow some noise reduction. The value of $m = 5$ gives a reasonable temporal profile of the second derivative but still noisy fluctuations in the third derivative (Fig. 13.6). The resulting model is better, but still invalid, since it exhibits a periodic behaviour rather than a chaotic one (Fig. 13.7). The value of $m = 12$ gives the best results: reasonable profiles of all the derivatives (Fig. 13.8), a much smaller approximation error $\varepsilon_{\text{rel}} = 0.07$ and a chaotic dynamics which is qualitatively very similar to the observed one (Fig. 13.9). A further increase in m worsens the results. Thus, at $m = 40$ the derivative estimates look even "smoother" (Fig. 13.10b–d) and the signal itself becomes somewhat distorted (Fig. 13.10a shows the difference between the original data and a smoothed signal $\hat{x}'(t)$). Hence, the random errors in the derivative estimates are smaller, but

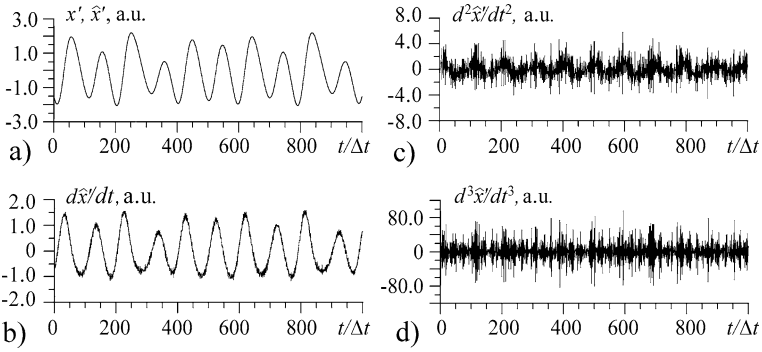

Fig. 13.4 Numerical differentiation of the signal $x'(t)$ with a digital smoothing polynomial at $m = 2$, $L = 3$: (**a**) an original signal $x'(t)$ and its smoothed estimate $\hat{x}'(t)$ fully coincide at this scale; (**b**)–(**d**) the derivatives of increasing order

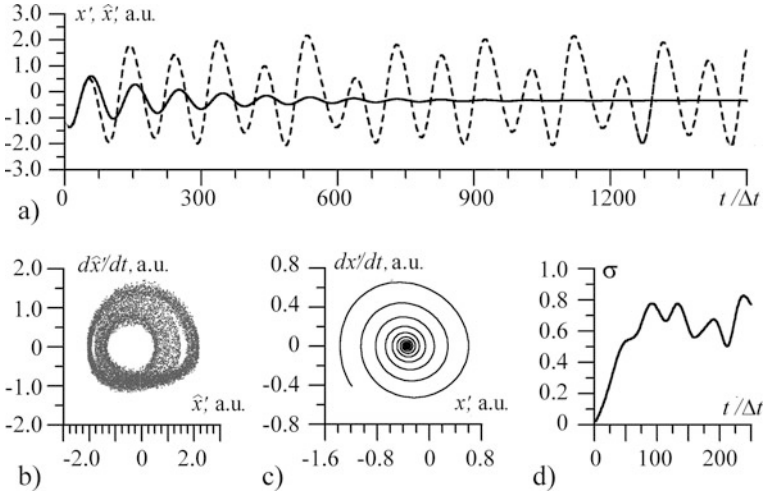

Fig. 13.5 Behaviour of an empirical model (13.8) obtained at $m = 2,\ L = 3$: (**a**) the test time series $x'(t)$ (the *dashed line*) and the model time realisation at the same initial conditions (the *solid line*); (**b**) a projection of the original data onto the plane $(\hat{x}', \mathrm{d}\hat{x}'/\mathrm{d}t)$; (**c**) a projection of the model phase orbit onto the same plane; (**d**) a model prediction error σ for the prediction $t/\Delta t$ sampling intervals ahead

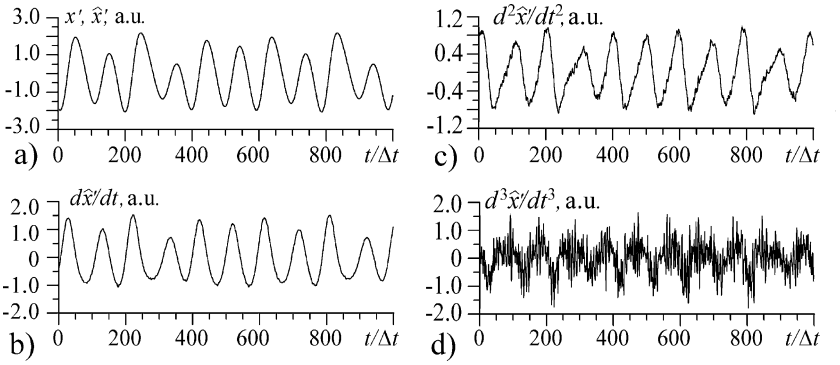

Fig. 13.6 Numerical differentiation of the signal $x'(t)$ at $m = 5,\ L = 3$. Notations are the same as in Fig. 13.4

there appears a significant bias. The corresponding model exhibits an approximation error greater than at $m = 12$ and a periodic behaviour (Fig. 13.11), which is not similar to the observed dynamics.

Big values of m can be used in combination with big values of L to allow the smoothing polynomial to reproduce the signal waveform in a wider window $\{t_n - m\Delta t; t_n + m\Delta t\}$. In particular, the pair $m = 40$ and $L = 7$ gives a model with chaotic behaviour and the best prediction time of $0.7T$ (even this prediction time is quite moderate, which is not surprising for a chaotic regime). However, a chaotic attractor of this model is less similar to the observed dynamics (it does not

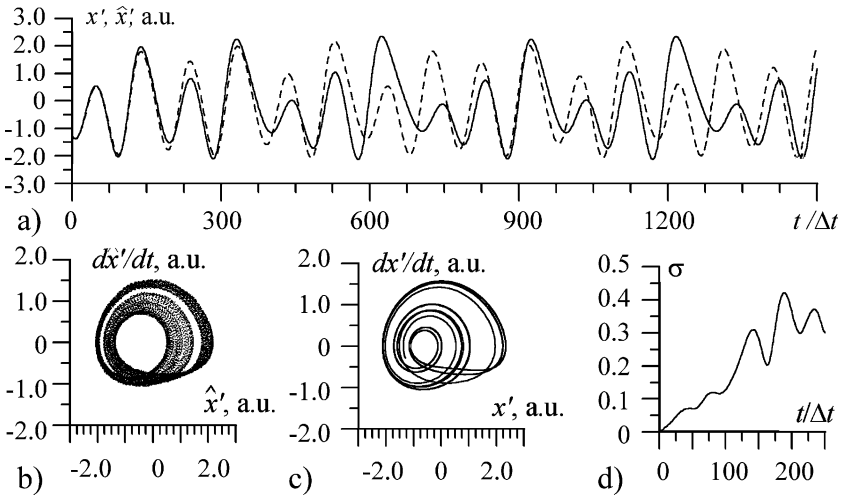

Fig. 13.7 Behaviour of an empirical model (13.8) obtained at $m = 5,\ L = 3$. Notations are the same as in Fig. 13.5

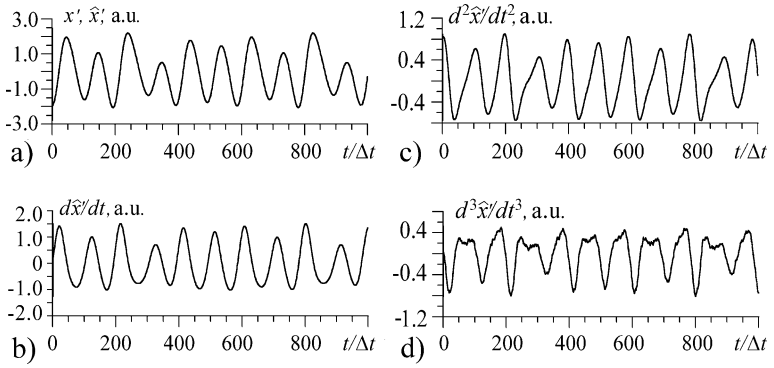

Fig. 13.8 Numerical differentiation of the signal $x'(t)$ at $m = 12,\ L = 3$. Notations are the same as in Fig. 13.4

exhibit a gap between the two bands seen in Fig. 13.9b, c) than that for the model obtained at $m = 12,\ L = 3$. However, the coefficients of both models are close to each other (Table 13.2). Below, we describe modelling of the coupled generators at $m = 12,\ L = 3$, since this choice has provided the best qualitative description of the chaotic dynamics of the generator 2. Still, both $m = 12,\ L = 3$ and $m = 40,\ L = 7$ appear to give very similar results of the coupling analysis.

13.1.4.2 Modelling of the Coupled Generators

The derivatives of $x(t)$ for the trial 4 are estimated also at $m = 12,\ L = 3$. Fitting the model equations (13.6), which involve the data from the generator 1 to describe

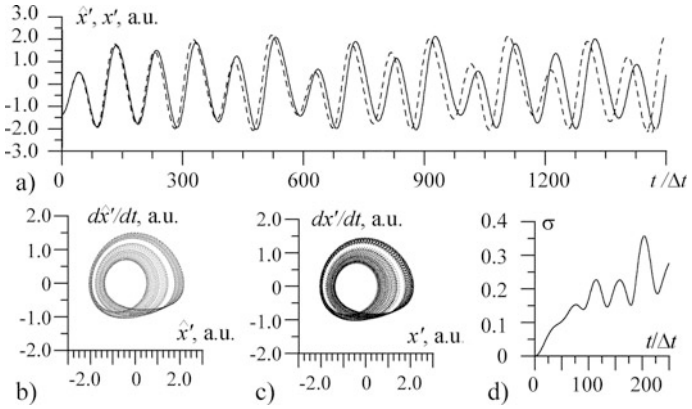

Fig. 13.9 Behaviour of an empirical model (13.8) obtained at $m = 12$, $L = 3$. Notations are the same as in Fig. 13.5

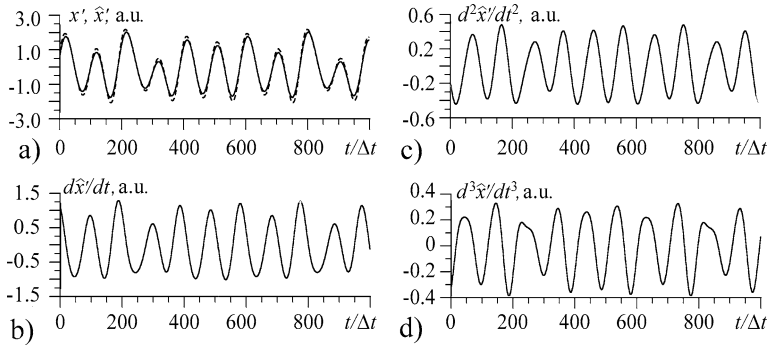

Fig. 13.10 Numerical differentiation of the signal $x'(t)$ at $m = 40$, $L = 3$. Notations are the same as in Fig. 13.4. An original signal $x'(t)$ in the panel *a* (the *dashed line*) somewhat differs from its smoothed estimate $\hat{x}'(t)$ (the *solid line*)

the time series of the generator 2, gives an approximation error $\varepsilon_{\text{rel}} = 0.07$, i.e. the same as for the individual model (13.8). The model coefficients responsible for the influence $1 \to 2$ appear close to zero: $\hat{c}'_6 = -0.001$ and $\hat{c}'_7 = 0.001$. The other coefficients are very close to the corresponding coefficients of the individual model. Thus, no quantitative improvement is observed under the use of the model (13.6) as compared to the model (13.8), i.e. one cannot see any signs of the influence $1 \to 2$.

As for the modelling of the generator 1, the results for the individual model (13.7) and the joint model (13.5) are reported in Table 13.3. One can see the reduction in the approximation error by 20% and the coupling coefficient estimate $\hat{c}_7$, which is not as small as that for the influence $1 \to 2$. Thus, some signs of coupling $2 \to 1$ are observed already from these characteristics. The presence of coupling and its unidirectional character becomes completely obvious when a free-run behaviour of different models is considered.

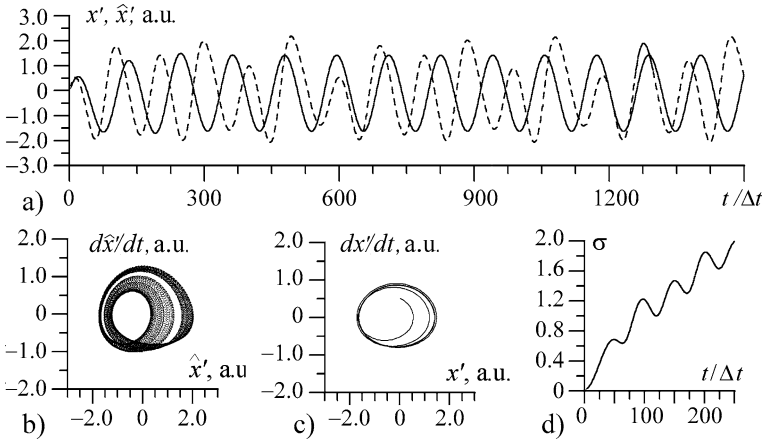

Fig. 13.11 Behaviour of an empirical model (13.8) obtained at $m = 40$, $L = 3$. Notations are the same as in Fig. 13.5

Table 13.3 Characteristics of models (13.5) and (13.7) for the generator 1

Model	$\hat{c}_1$	$\hat{c}_2$	$\hat{c}_3$	$\hat{c}_4$	$\hat{c}_5$	$\hat{c}_6$	$\hat{c}_7$	ε_{rel}
(13.7)	−0.28	−0.43	0.03	−0.23	0.13	–	–	0.15
(13.5)	−0.32	−0.43	0.03	−0.25	0.13	−0.002	0.006	0.12

Projections of the original and model phase orbits onto different planes are presented in Fig. 13.12. The observed dynamics of the generator 1 is illustrated in Fig. 13.12a. The individual model (13.7) gives a periodic regime (Fig. 13.12b), i.e. it is inadequate. The model allowing for unidirectional coupling $2 \to 1$, i.e. Eqs. (13.5) and (13.8), exhibits a chaotic attractor very similar to the observed behaviour (Fig. 13.12c). A model with bidirectional coupling, i.e. Eqs. (13.5) and (13.6), does not give any further improvement (Fig. 13.12d). The results for the generator 2 are presented similarly in the second row. Already the individual model (13.8) adequately reproduces the dynamics (cf. Fig. 13.12e and f). A model with a unidirectional coupling $1 \to 2$, i.e. Eqs. (13.7) and (13.6), and a model with a bidirectional coupling demonstrate the same behaviour (Fig. 13.12g, h). Similar conclusions are made from the projections onto the plane (x, x'): the model with unidirectional coupling $1 \to 2$ is insufficient to reproduce the dynamics qualitatively (cf. Fig. 13.12i and j), while the model with unidirectional coupling $2 \to 1$ (Fig. 13.12k) and the model with bidirectional coupling (Fig. 13.12l) exhibit the same dynamics similar to the observed one.

Thus, via the analysis of a free-run behaviour of the empirical models and their approximation errors, we infer from data that the unidirectional coupling scheme $2 \to 1$ is realised in the trial 4. This is a correct conclusion. In this manner, the global modelling helps both to get an adequate model, when parameters of the circuits are unknown, and to reveal the coupling scheme. Similar results are observed

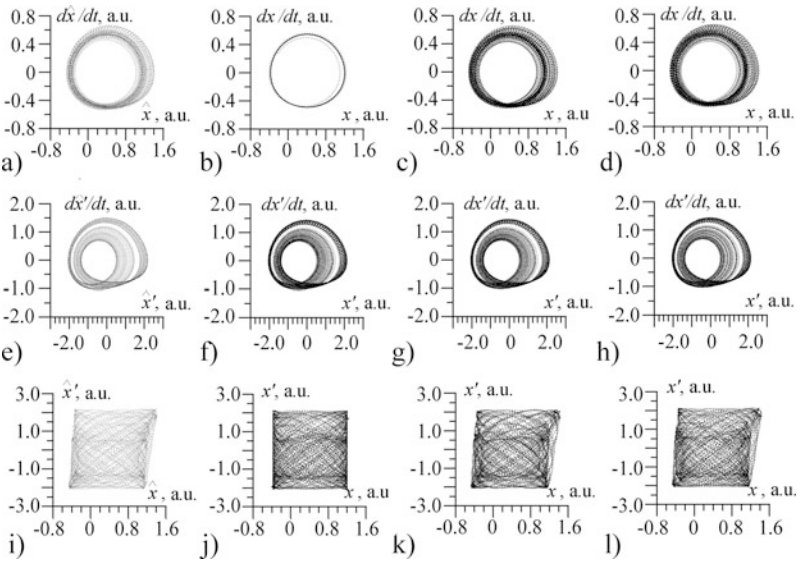

Fig. 13.12 Comparison of the original data and a behaviour of different empirical models obtained at $m = 12,\ L = 3$: (**a**), (**e**), (**i**) projections of the original data for the test time series; (**b**) a model (13.7), no coupling; (**c**), (**k**) models (13.5) and (13.8), i.e. a unidirectional coupling $2 \rightarrow 1$ is allowed for; (**d**), (**h**), (**l**) models (13.5) and (13.6), i.e. a bidirectional coupling is allowed for; (**f**) a model (13.8), no coupling; (**g**), (**j**) models (13.7) and (13.6), i.e. a unidirectional coupling $1 \rightarrow 2$ is allowed

for all seven trials (Table 13.1). The results in terms of the approximation error are summarised in Fig. 13.13, where we use $m = 40,\ L = 7$, since this choice always gives a good description of the dynamics, while the choice of $m = 12,\ L = 3$ is the best one for the trial 4 and a couple of other cases (anyway, the results are very

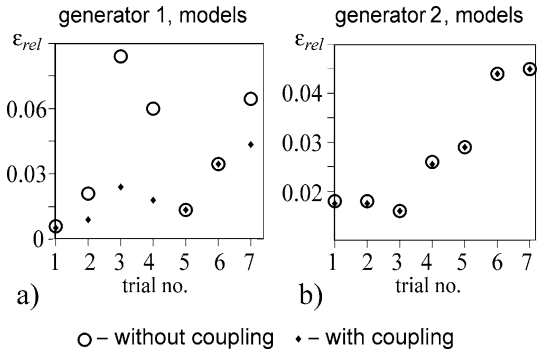

Fig. 13.13 Relative approximation errors for the models without coupling (*circles*) and allowing for a unidirectional coupling (rhombs) at $m = 40,\ L = 7$: (**a**) the models (13.7) and (13.5) for the generator 1; (**b**) the models (13.8) and (13.6) for the generator 2

similar for these two choices of the pair *m,L*). A unidirectional coupling $2 \rightarrow 1$ is correctly detected in the trials 2, 3, 4 and 7: the reduction in the approximation error is observed for the model (13.5), since the rhombs are located considerably lower than the circles. No coupling is detected in the other three trials, which is also correct. The same conclusions are obtained when we compare the prediction times or consider the projections of the model phase orbits (not shown).

Finally, we note that the trial 3 corresponds to a phase synchronisation regime: the phases of the generators are locked, but variations in their instantaneous amplitudes are a bit different due to the non-identity of the circuits (a slight parameter mismatch). Coupling character cannot be revealed from the locked phases with the phase dynamics modelling technique (Sect. 12.2). The Granger causality estimation may also face difficulties, since an inappropriate model structure in the case of a strong unidirectional coupling may lead to a spurious detection of a bidirectional coupling. Fitting the models (13.5) and (13.6) allows one to reveal the coupling character correctly even in this case due to the adequate model structure (and due to non-identity of the amplitude variations). This is an advantage of the situation when detailed a priori information about an object is available: a further useful knowledge can be extracted then from minimally informative experimental data.

Thus, with the electronic example we have illustrated the full procedure of constructing an empirical model under the "transparent box" setting and revealing a coupling character with its help.

13.2 Parkinsonian Tremor

13.2.1 Object Description

As mentioned in Sect. 12.3, one of the manifestations of Parkinson's disease is a strong resting tremor, i.e. regular high-amplitude oscillations of limbs. The mechanism of the parkinsonian tremor is still widely discussed. It is known that populations of neurons located in the thalamus and the basal ganglia fire in a synchronised and periodical manner at a frequency similar to that of the tremor (Lenz et al., 1994; Llinas and Jahnsen, 1982; Pare et al., 1990) as a result of local pathophysiology. Also, there is an important peripheral mechanism involved in the generation of these abnormal oscillations: the receptor properties in the muscle spindles. They contribute to a servo control (closed-loop control of position and velocity) and amplify synchronised input from central nervous structures by strongly synchronised feedback (Stilles and Pozos, 1976). The resulting servo loop oscillations are regarded as a basic mechanism for tremor generation (Stilles and Pozos, 1976). Although subcortical oscillations are not strictly correlated with the tremor (Rivlin-Etzion et al., 2006), it was shown that limb oscillations influence subcortical activity by the proprioceptive feedback from muscle spindles (Eichler, 2006). As yet, it was difficult to reveal empirically whether the parkinsonian tremor is affected by subcortical oscillations (Brown, 2003; Rivlin-Etzion et al., 2006).

For deeper understanding of the mechanism of the parkinsonian tremor generation, it is important to reveal the character of interaction between different brain areas and oscillating limbs. Due to the regularity of the parkinsonian tremor, application of the phase dynamics modelling technique (Sect. 12.2) has appeared fruitful (Bezruchko et al., 2008; Smirnov et al., 2008). Namely, a bidirectional coupling between limb and subcortical oscillations has been detected and time delays in both directions have been estimated. Below, we describe such an analysis of a single tremor epoch in a patient with bilateral resting tremor. The patient had more pronounced pathological oscillations of the left hand.

13.2.2 Data Acquisition and Preliminary Processing

Local field potentials (LFPs) from the subthalamic nucleus (STN) and accelerometer signals, assessing the hand tremor, were recorded simultaneously. It was done by the group of Prof. P. Tass (Institute of Neuroscience and Biophysics – 3, Research Centre Juelich, Germany) and their colleagues at the Department of Stereotaxic and Functional Neurosurgery, University of Cologne. Recordings were performed during or after deep brain stimulation electrode implantation. Intraoperative recordings from the right STN were performed with the ISIS MER system (Inomed, Teningen, Germany). The latter is a "Ben's gun" multi-electrode for acute basal ganglia recordings during stereotaxic operations (Benabid et al., 1987), i.e. an array consisting of four outer electrodes separated by 2 mm from a central one. Proper electrode placement was confirmed by effective high-frequency macro-stimulations, intraoperative X-ray controls (Treuer et al., 2005), postoperative CT scans and intraoperative micro-recordings. The LFP recordings represented voltages on the depth electrodes against a remote reference. The recordings were performed after overnight withdrawal of antiparkinsonian medication. The study was approved by the local ethical committee. The patient gave a written consent.

Accelerometer and LFP signals are denoted further as $x_1(t)$ and $x_2(t)$, respectively, where $t = n\Delta t$, $n = 1, 2, \ldots$, the sampling interval is $\Delta t = 5$ ms. An accelerometer signal from the left hand during an epoch of strong resting tremor (of the length of 83.5 s or 16700 data points) is shown in Fig. 13.14a. The simultaneous LFP recording performed via the central depth electrode is shown in Fig. 13.14b. We describe only the central electrode, since all the results are very similar for all depth electrodes. The accelerometer signal displays a sharp peak in the power spectrum (Fig. 13.14c) at the frequency of 5 Hz. The corresponding spectral peak in the power spectrum of LFP is also observed (Fig. 13.14d). A spectral peak at the tremor frequency is often manifested in the power spectrum of the LFP recorded from the depth electrode contralateral to (i.e. at the opposite side of) the tremor (Brown, 2003; Deuschl et al., 1996; Rivlin-Etzion et al., 2006; Zimmermann et al., 1994).

The parkinsonian resting tremor is highly regular: the peak at the tremor frequency is rather narrow for the accelerometer signal. The peak in the LFP power spectrum is wider. This regularity is further illustrated by the autocorrelation

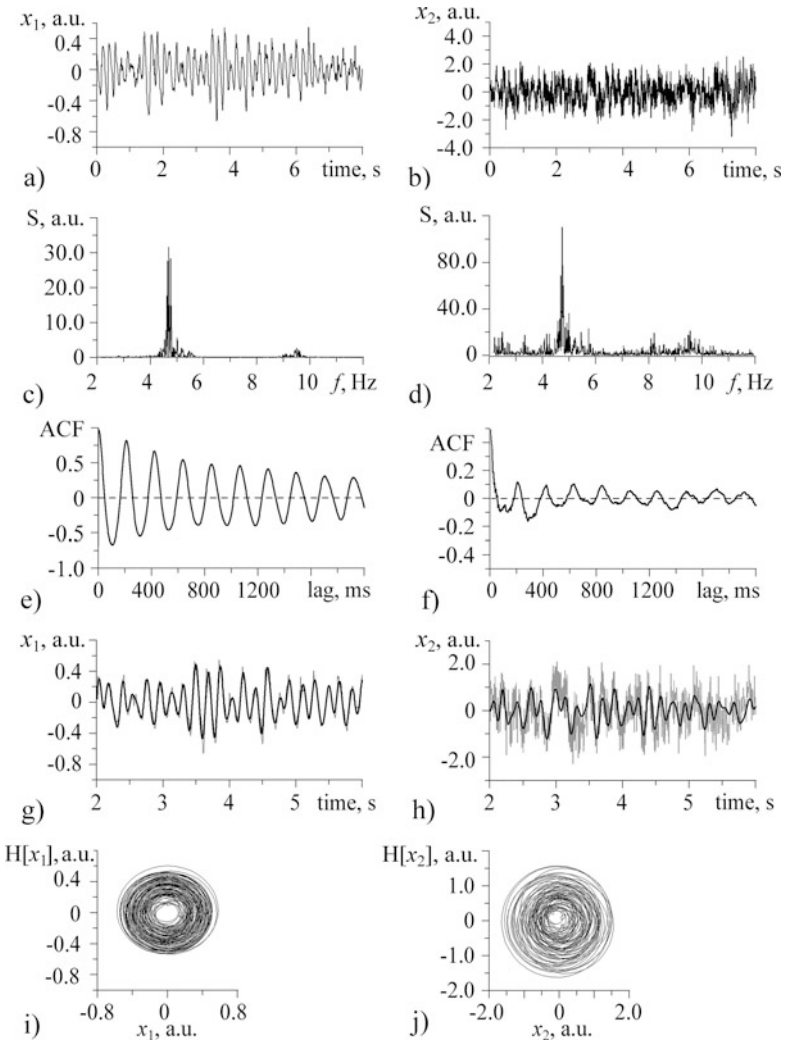

Fig. 13.14 A spontaneous epoch of parkinsonian tremor of length 83.5 s. The left column relates to an accelerometer signal and the right one to a simultaneous LFP signal: (**a**), (**b**) the time series at the beginning of the epoch; (**c**), (**d**) their power spectra estimates (periodograms); (**e**), (**f**) their autocorrelation functions; (**g**), (**h**) magnified segments of the original signals (*grey lines*) and their versions band-pass filtered (*black lines*) in the frequency band 2–9 Hz; (**i**), (**j**) the orbits on the plane "a band-pass filtered signal (2–9 Hz) versus its Hilbert transform"

functions in Fig. 13.14e, f: the ACF of x_1 (Fig. 13.14e) decays much slower than that of x_2 (Fig. 13.14f). A signal with a strong periodic component is often called "phase coherent", since the phases of two orbits with initially the same phase diverge very slowly in time (see, e.g., Pikovsky et al., 2001). In such a case, one speaks also of

weak phase diffusion, which is manifested as weak variations in the instantaneous period (a time interval between successive local maxima in a time series). The phase diffusion can be characterised by the coefficient of variation of the instantaneous period $k = \sqrt{\langle (T_i - \langle T_i \rangle)^2 \rangle} \Big/ \langle T_i \rangle$, where T_i are the intervals between successive maxima ($i = 1, 2, \ldots$) and angle brackets denote averaging over the time index i. For the accelerometer signal shown in Fig. 13.14a, the value of k is equal to 0.05 (local maxima and the distances T_i are determined from a band-pass filtered signal, shown by the black line Fig. 13.14g, to avoid fast fluctuations inappropriate for the determination of the tremor period). Since the instantaneous period varies only by 5% as compared to its mean value of $\langle T_i \rangle \approx 200$ ms, the process can be regarded as rather phase coherent. Our analysis of 41 tremor epochs from three different patients (Smirnov et al., 2008) shows that the coefficient k for the accelerometer signals typically takes the values of 0.05–0.1. For such regular signals, it is most reasonable to introduce phases and estimate couplings via the phase dynamics modelling as justified in Smirnov and Andrzejak (2005) and Smirnov et al. (2007).

Before the phase dynamics modelling, it is necessary to select a frequency band to define the phases. The results may differ for different bands. Inclusion of the frequencies below 2–3 Hz may shift the focus to slow processes like the heart beat or technical trends, which are not related to the parkinsonian tremor generation. Inclusion of the frequencies higher than 9–10 Hz implies a description of fast fluctuations, in particular, higher harmonics of the basic frequency. Such fluctuations may play a role of noise in the modelling of the tremor and make confident conclusions about the coupling presence more difficult. However, all that is not known in advance. Hence, one must try different frequency bands. We present the results only for a rather wide frequency band around the tremor frequency and then briefly comment what differs if other bands are used.

Both signals $x_1(t)$ and $x_2(t)$ are filtered in the relatively wide frequency band of 2–9 Hz (Fig. 13.14g, h). Their Hilbert transforms (Sect. 6.4.3) are illustrated in Fig. 13.14i, j, where rotation about a clearly defined centre is seen for both signals. Thus, the phases $\phi_1(t)$ and $\phi_2(t)$ are defined reasonably well. Ten characteristic periods at both edges of the phase time series are removed from the further analysis, since the corresponding phase values may be strongly distorted due to the edge effects as discussed in Pikovsky et al. (2000). The resulting phase time series of length 15900 data points (approximately 400 oscillation periods) is used for model fitting.

The cross-correlation function between the LFP and the contralateral hand acceleration is shown in Fig. 13.15a. Within a range of time lags, the CCF significantly differs from zero. Thus, the presence of coupling can be inferred reliably already from the CCF. The CCF exhibits some asymmetry: local maximum of its absolute value, closest to zero time lag, is observed at -25 ms. It could be a sign that the signal $x_2(t)$ "leads". However, somewhat higher peaks are observed at positive time lags, more distant from zero. Thus, directional coupling characteristics cannot be extracted from the CCF unambiguously, which is a typical case.

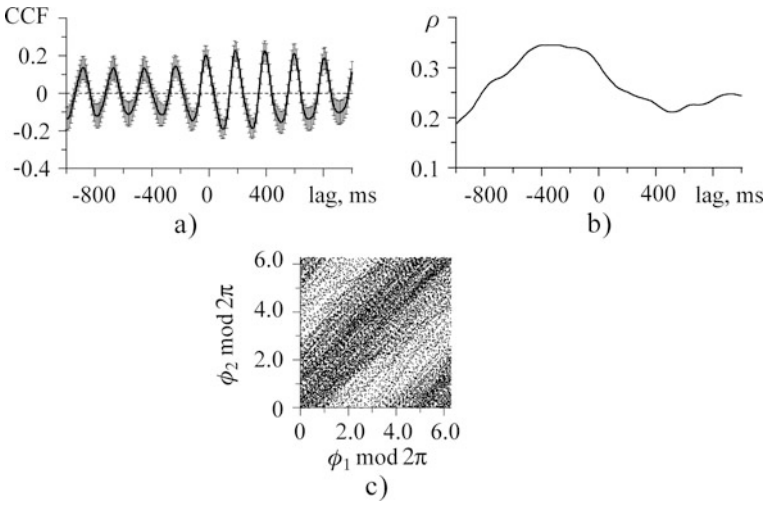

Fig. 13.15 Simple characteristics of interdependence between the accelerometer and LFP signals, shown in Fig. 13.14: (**a**) the cross-correlation function, error bars show the 95% confidence bands estimated via Bartlett's formula (Bartlett, 1978); (**b**) phase synchronisation index for the phases defined in the frequency band 2–9 Hz; (**c**) the data points on the plane of wrapped phases

13.2.3 Selection of the Model Equation Structure

At variance with the electronic example (Sect. 13.1), model equations for the parkinsonian tremor and subcortical activity cannot be written down from physical or physiological considerations. Thus, the structure of model equations cannot be regarded as completely known. On the other hand, it has appeared possible to introduce the phases of the oscillations related to the tremor frequency band. As discussed in Sect. 12.2, an adequate description of the phase dynamics for a wide range of oscillatory processes is achieved with the phase oscillator model, i.e. a first-order stochastic differential equation (Kuramoto, 1984; Rosenblum et al., 2001). For two processes, the model reads as

$$\begin{aligned} \mathrm{d}\phi_1(t)\big/\mathrm{d}t &= \omega_1 + G_1(\phi_1(t), \phi_2(t-\Delta_{2\to1})) + \xi_1(t), \\ \mathrm{d}\phi_2(t)\big/\mathrm{d}t &= \omega_2 + G_2(\phi_2(t), \phi_1(t-\Delta_{1\to2})) + \xi_2(t), \end{aligned} \tag{13.9}$$

where ω_k is the angular frequency, the function G_k is 2π periodic with respect to both arguments, $\Delta_{2\to1}$, $\Delta_{1\to2}$ are time delays in couplings, ξ_k are zero-mean white noises with ACFs $\langle \xi_k(t)\xi_k(t')\rangle = \sigma^2_{\xi_k}\delta(t-t')$, $\sigma^2_{\xi_k}$ characterises noise intensity. Empirical model is convenient to be sought for in the form of the corresponding difference equations:

$$\begin{aligned} \phi_1(t+\tau) - \phi_1(t) &= F_1(\phi_1(t), \phi_2(t-\Delta_{2\to1}), \mathbf{a}_1) + \varepsilon_1(t), \\ \phi_2(t+\tau) - \phi_2(t) &= F_2(\phi_2(t), \phi_1(t-\Delta_{1\to2}), \mathbf{a}_2) + \varepsilon_2(t), \end{aligned} \tag{13.10}$$

where τ is the fixed time interval equal to the basic oscillation period (200 ms in our case), ε_k is the zero-mean noise, F_k is the third-order trigonometric polynomial (12.8), $\mathbf{a}_k$ is the vector of its coefficients, $\Delta_{2\to1}$, $\Delta_{1\to2}$ are trial time delays.

Thus, a suitable model structure (or, at least, a good guess for it) for the phases of the processes $x_1(t)$ and $x_2(t)$ can be considered as partly known due to relatively high regularity of the processes. Indeed, the first-order difference equation (13.10) with low-order trigonometric polynomials is a sufficiently universal choice, but not as arbitrary as in the black box case (Chap. 10): one does not need to try different model dimensions and different types of approximating functions.

13.2.4 Model Fitting, Validation and Usage

The three conditions of applicability of the phase dynamics modelling technique (Smirnov and Bezruchko, 2003; 2009) are imposed on the time series length (not less than 40 characteristic periods), the synchronisation index (not greater than 0.45) and the autocorrelation function of the model residual errors (the ACF decreases down to 0 or, at least, gets less than 0.2, over the interval of time lags up to τ). In our example, the length of the considered time series is about 400 characteristic oscillation periods, which is sufficiently big. Phase synchronisation index

$$\rho(\Delta) = \left| \frac{1}{N} \sum_{n=1}^{N} e^{i(\phi_1(n\Delta t) - \phi_2(n\Delta t + \Delta))} \right|$$

is less than 0.4 for any time lag Δ (Fig. 13.15b) as required. Sufficiently weak interdependence between simultaneous values of ϕ_1 and ϕ_2 is also illustrated in Fig. 13.5c: the distribution of the observed values on the plane of the wrapped phases fills the entire square and exhibits only weak non-uniformity. The ACF of the residual errors must be checked after fitting the model (13.10) to the phase time series.

We have fitted the equations to the data as described in Sect. 12.2. Namely, we have fixed $\tau = 200$ ms and minimised mean-squared approximation errors

$$\hat{\sigma}^2_{k,\mathbf{a}}(\Delta_{j\to k}, \mathbf{a}_k) = \frac{1}{N - \tau/\Delta t} \sum_{n=\tau/\Delta t+1}^{N} \big(\phi_k(n\Delta t + \tau) - \phi_k(n\Delta t) - F_k(\phi_k(n\Delta t), \phi_j(n\Delta t - \Delta_{j\to k}), \mathbf{a}_k)\big)^2,$$

where $k, j = 1, 2$ $(j \neq k)$. For a fixed value of the trial delay $\Delta_{j\to k}$, this is a linear problem so that the coefficient estimates $\hat{\mathbf{a}}_k(\Delta_{j\to k}) = \arg\min_{\mathbf{a}_k} \hat{\sigma}^2_{k,\mathbf{a}}(\Delta_{j\to k}, \mathbf{a}_k)$ are found by solving a linear set of algebraic equations. The minimisation is performed for different trial delays. Then, the quantity $\hat{\sigma}^2_k(\Delta_{j\to k}) = \min_{\mathbf{a}_k} \hat{\sigma}^2_{k,\mathbf{a}}(\Delta_{j\to k}, \mathbf{a}_k)$ is plotted versus $\Delta_{j\to k}$ (Fig. 13.16a, b). Its minimal value characterises the phase

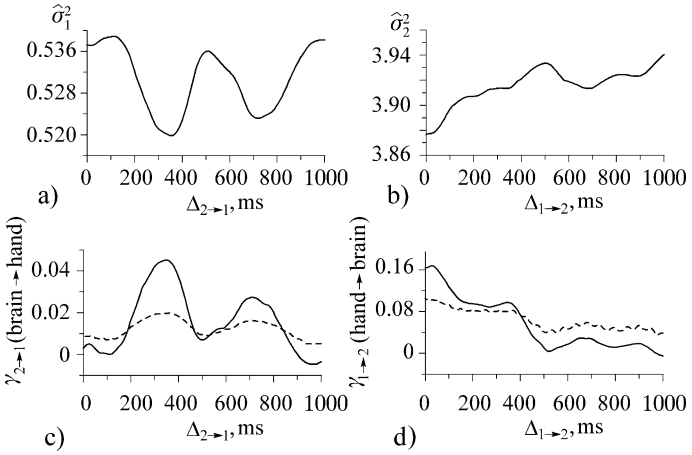

Fig. 13.16 Fitting the phase dynamics model (13.10) to the data of Fig. 13.14: (**a**), (**b**) approximation errors $\hat{\sigma}_1^2$ and $\hat{\sigma}_2^2$ (dimensionless) versus a trial time delay; (**c**), (**d**) coupling characteristics $\gamma_{2\to1}$ and $\gamma_{1\to2}$ (dimensionless) versus a trial time delay (*solid lines*) along with the pointwise 0.975 quantiles $\gamma_{2\to1,c}$ and $\gamma_{1\to2,c}$ (*dashed lines*)

diffusion intensity: $\hat{\sigma}^2_{k,\min} = \min\limits_{\Delta_{j\to k}} \hat{\sigma}^2_k(\Delta_{j\to k})$. From the coefficient estimates $\hat{\mathbf{a}}_k$, the coupling strength $\gamma_{j\to k}(\Delta_{j\to k})$ is computed as their weighted sum. The formula for $\gamma_{j\to k}$ is given in Sect. 12.2. For the low-order trigonometric polynomials used, it appears that the maximum of $\gamma_{j\to k}(\Delta_{j\to k})$ corresponds to the minimum of $\hat{\sigma}^2_k(\Delta_{j\to k})$ (Fig. 13.16c, d).

The formula for the critical value $\gamma_{j\to k,c}(\Delta_{j\to k})$, which is a pointwise 0.975 quantile for the estimator $\gamma_{j\to k}(\Delta_{j\to k})$ in the case of uncoupled processes, is also available (Sect. 12.2). If one observes that $\gamma_{j\to k}(\Delta_{j\to k}) > \gamma_{j\to k,c}(\Delta_{j\to k})$ for a range of time delays wider than half a basic oscillation period (for an entire tried range of time delays covering five basic periods), then the presence of coupling can be inferred at the resulting significance level of 0.05 (i.e. with a probability of random error less than 0.05). This is the case in our example (Fig. 13.16c, d). Thus, a bidirectional coupling between the brain activity and the limb oscillations is detected.

Then, the location of the maximum of $\gamma_{j\to k}(\Delta_{j\to k})$ or the minimum of $\hat{\sigma}^2_k(\Delta_{j\to k})$ gives an estimate of the time delay: $\hat{\Delta}_{j\to k} = \arg\min\limits_{\Delta_{j\to k}} \hat{\sigma}^2_k(\Delta_{j\to k})$. In our case, the estimated time delay is $\hat{\Delta}_{2\to1} = 350$ ms for the influence $2 \to 1$ (brain to hand, $\gamma_{2\to1}(\hat{\Delta}_{2\to1}) = 0.045$) and $\hat{\Delta}_{1\to2} = 0$ ms for the influence $1 \to 2$ (hand to brain, $\gamma_{1\to2}(\hat{\Delta}_{1\to2}) = 0.16$).

Finally, the obtained model (13.10) with coefficients $\hat{\mathbf{a}}_k(\hat{\Delta}_{j\to k})$ should be validated including the properties of its residual errors. Our optimal model is specified by the phase diffusion intensities $\hat{\sigma}^2_{1,\min} = 0.52$ and $\hat{\sigma}^2_{2,\min} = 3.88$, and the following significantly non-zero coefficients (see their notations in Sect. 12.2): $w_1 = 6.03 \pm 0.07$, $\beta_{1,2,0} = 0.019 \pm 0.017$, $\alpha_{1,1,1} = 0.213 \pm 0.076$;

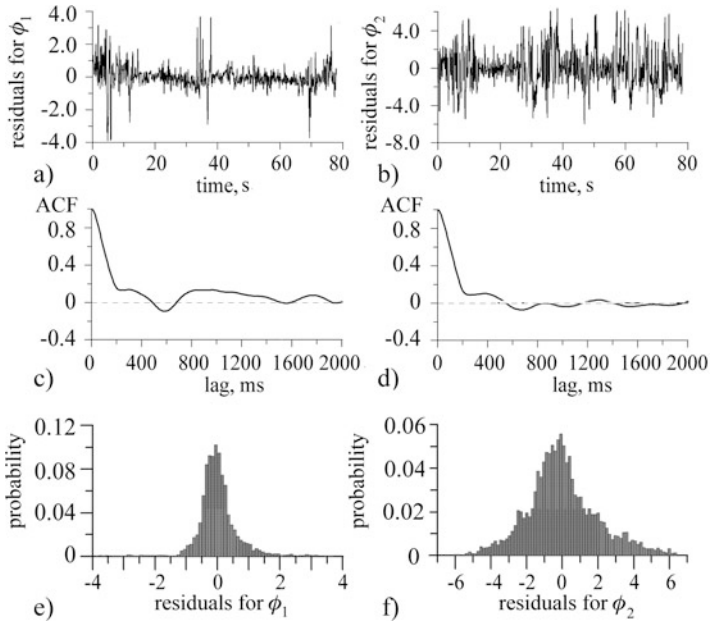

Fig. 13.17 Residual errors of the optimal phase dynamics model (13.10) for the epoch of Fig. 13.14. The left column shows residuals for the accelerometer signal phase, the right one is for the LFP signal phase: (**a**), (**b**) residual errors versus time; (**c**), (**d**) their autocorrelation functions; (**e**), (**f**) their histograms

$w_2 = 6.28 \pm 0.20$, $\beta_{2,1,1} = 0.44 \pm 0.21$. Time realisations of this model represent almost linear increase of the phases with some fluctuations. Qualitatively, they are very similar to the observed almost linearly increasing phases (not shown, since the plots are not informative). The model residuals are shown in Fig. 13.17a, b and their ACFs in Fig. 13.17c, d. The ACFs get less than 0.2 for time lags greater than $\tau = 200$ ms as required. Thus, applicability of the technique is confirmed.

The required properties of the residuals and proper behaviour of the time realisations validate the obtained model (13.10). The main usage of the model in our case is to make conclusions about the couplings between the processes. As already mentioned, it reveals a bidirectional coupling. Further, for the time series considered, the brain-to-hand influence appears delayed by more than a basic oscillation period, while the opposite influence is non-delayed. These results appear reproducible (another tremor epoch is illustrated in Figs. 12.1 and 12.2): the analysis of 41 tremor epochs from three different patients (Smirnov et al., 2008) in 30 cases has revealed the "coupling pattern" similar to that in Fig. 13.16, i.e. a bidirectional coupling which is significantly time delayed in the brain-to-hand direction and almost non-delayed in the opposite direction. In the other 11 epochs, no coupling has been detected. The cause seems to be that epochs of strong tremor occur intermittently in all the patients and the estimated curves $\gamma_{j\to k}(\Delta_{j\to k})$ fluctuate stronger for shorter epochs. It can be interpreted as an effect of noise. Averaging over all tremor epochs

available for a given patient exhibits the plots $\gamma_{j\to k}(\Delta_{j\to k})$ shown in Fig. 12.3, which clearly confirm the coupling pattern observed in Fig. 13.16.

The results do not change under sufficiently strong variations in the frequency band used to define the phases. Namely, the results are practically the same if the lower cut-off frequency is not less than 2 Hz and not greater than $f_{\text{tremor}} - f_c$ and the upper cut-off frequency is not less than $f_{\text{tremor}} + f_c$ and not greater than $2f_{\text{tremor}} - f_c$, where f_{tremor} is the basic tremor frequency and f_c is equal to 1 Hz. In our example, $f_{\text{tremor}} = 5$ Hz so that the acceptable values of the lower cut-off frequency range from 2 to 4 Hz and those of the upper cut-off frequency are from 6 to 9 Hz. Above, we have presented the results for a maximally wide acceptable frequency band. Its further enlargement or movement to higher frequencies gives less regular signals (a stronger phase diffusion) and insignificant conclusions about the coupling presence.

13.2.5 Validation of Time Delay Estimation

An analytic formula for the error in the time delay estimates is unavailable. To check correctness of the time delay estimation and assess its typical errors, we apply the same modelling procedure to a toy model consisting of the noisy van der Pol oscillator (an "analogue" of the hand oscillations) and a strongly dissipative linear oscillator (an "analogue" of the brain signal). Parameters of these oscillatory systems are selected so that they give stronger phase diffusion for the "LFP" signals and weaker one for the "tremor" signals as it is observed for the measurement data. Thus, the accelerometer ($a_1(t) = \mathrm{d}^2 y_1(t)/\mathrm{d}t^2$) and LFP ($y_2(t)$) model oscillators read as

$$\begin{aligned}
&\frac{\mathrm{d}^2 y_1(t)}{\mathrm{d}t^2} - \left(\lambda - y_1^2(t)\right)\frac{\mathrm{d}y_1(t)}{\mathrm{d}t} + y_1(t) = k_{2\to 1}(y_2(t-\tau_{2\to 1}) - y_1(t)) + \xi_1(t),\\
&\frac{\mathrm{d}^2 y_2(t)}{\mathrm{d}t^2} + 0.15\frac{\mathrm{d}y_2(t)}{\mathrm{d}t} + y_2(t) = k_{1\to 2}(y_1(t-\tau_{1\to 2}) - y_2(t)) + \xi_2(t), \quad (13.11)
\end{aligned}$$

where ξ_1, ξ_2 are independent white noises with ACFs $\langle \xi_k(t)\xi_k(t')\rangle = \sigma_{\xi_k}^2 \delta(t-t')$, $\sigma_{\xi_1} = \sigma_{\xi_2} = 0.1$, $\lambda = 0.05$ and $\tau_{2\to 1}, \tau_{1\to 2}$ are time delays. Angular frequencies of both oscillators are approximately equal to 1 so that their periods are about six time units. To generate a time series, the equations are integrated with the Euler technique (Sect. 4.5.2) at the step size of 0.01. The sampling interval is equal to 0.15, i.e. gives approximately 40 data points per basic period of oscillations.

The reasoning behind the simple model equation (13.11) is as follows. Firstly, the non-linear oscillator is chosen as a model of the accelerometer signal, since in a large number of tremor epochs our attempts to reconstruct a model equation from an accelerometer time series resulted in similar models (not shown). In fact, the spinal cord is able to produce self-sustained rhythmic neural and muscular activity due to its central pattern generators (Dietz, 2003). Moreover, similar models were previously obtained both for parkinsonian and essential tremor dynamics (Timmer

et al., 2000). We consider the oscillator which is close to the point of the Andronov – Hopf bifurcation and demonstrates self-sustained oscillations (positive value of λ) perturbed by noise. However, the coupling estimation results are very similar for small negative λ, since the noise induces similar oscillations for small negative and small positive values of λ. Secondly, the linear oscillator is chosen as a model of the LFP signal, since construction of polynomial autoregressive models with different polynomial orders did not detect pronounced non-linearity (not shown).

The time series and power spectra estimates for the coupled oscillators (13.11) are shown in Fig. 13.18 (cf. Fig. 13.14).

We have analysed ensembles of time series generated by equation (13.11) with exactly the same procedure as applied to the experimental data above. In the numerical simulations, we used ensembles consisting of 100 time series of length of 100 basic periods. The results for a single epoch of Fig. 13.18 are shown in Figs. 13.19 and 13.20: they are qualitatively similar to the corresponding experimental results in Figs. 13.16 and 13.17. The averaged plots of coupling estimates for the observables $a_1(t)$ and $y_2(t)$ are shown in Fig. 13.21 in the same form as for the experimental results in Fig. 12.3. Without coupling (i.e. for $k_{2\to1} = k_{1\to2} = 0$), Fig. 13.21a, b

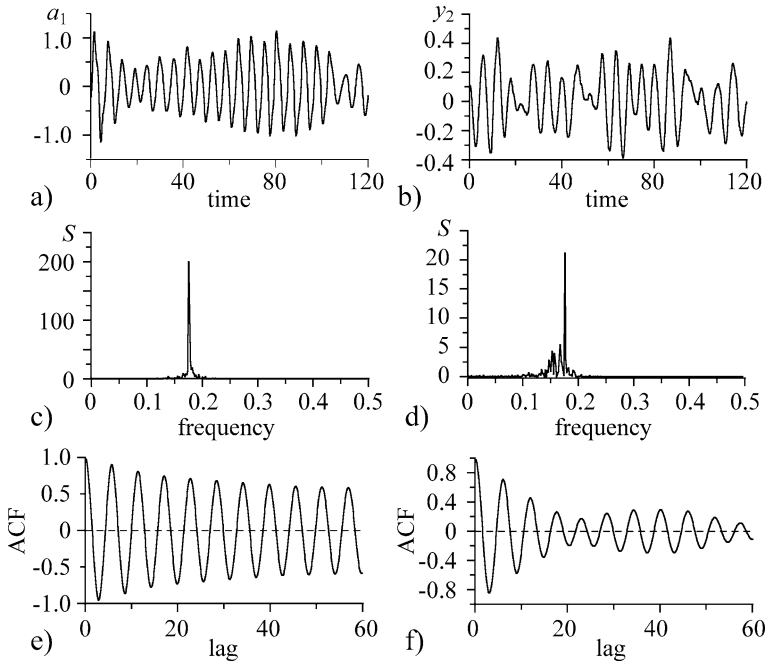

Fig. 13.18 A simulated time realisation of equation (13.11) of the duration 600 units of time t (4000 data points, about 100 basic periods) for the parameters $k_{2\to1} = 0.2$, $\tau_{2\to1} = 13.0$, $k_{1\to2} = 0.05$, $\tau_{1\to2} = 0$: (**a**) a signal $a_1(t) = \mathrm{d}^2 y_1(t) \,/ \mathrm{d}t^2$ at the beginning of the epoch considered, an analogue of the band-pass-filtered accelerometer signal $x_1(t)$ (Fig. 13.14g); (**b**) a simultaneous signal $y_2(t)$, an analogue of the band-pass-filtered LFP $x_2(t)$ (Fig. 13.14h); (**c**), (**d**) periodograms of $a_1(t)$ and $y_2(t)$, respectively; (**e**), (**f**) their autocorrelation functions

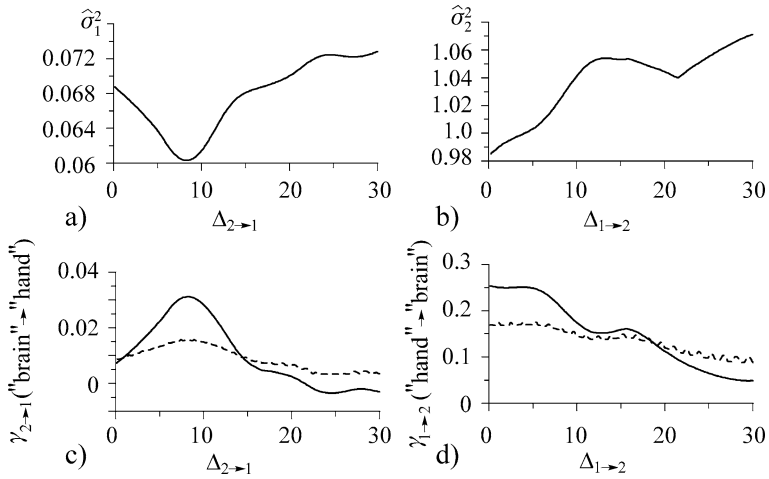

Fig. 13.19 Fitting the phase dynamics equation (13.10) to the time realisations of the model (13.11) illustrated in Fig. 13.18: (**a**), (**b**) the approximation errors $\hat{\sigma}_1^2$ and $\hat{\sigma}_2^2$ versus a trial time delay; (**c**), (**d**) the coupling characteristics $\gamma_{2\to1}$ and $\gamma_{1\to2}$ versus a trial time delay (*solid lines*) along with the pointwise 0.975 quantiles $\gamma_{2\to1,c}$ and $\gamma_{1\to2,c}$ (*dashed lines*)

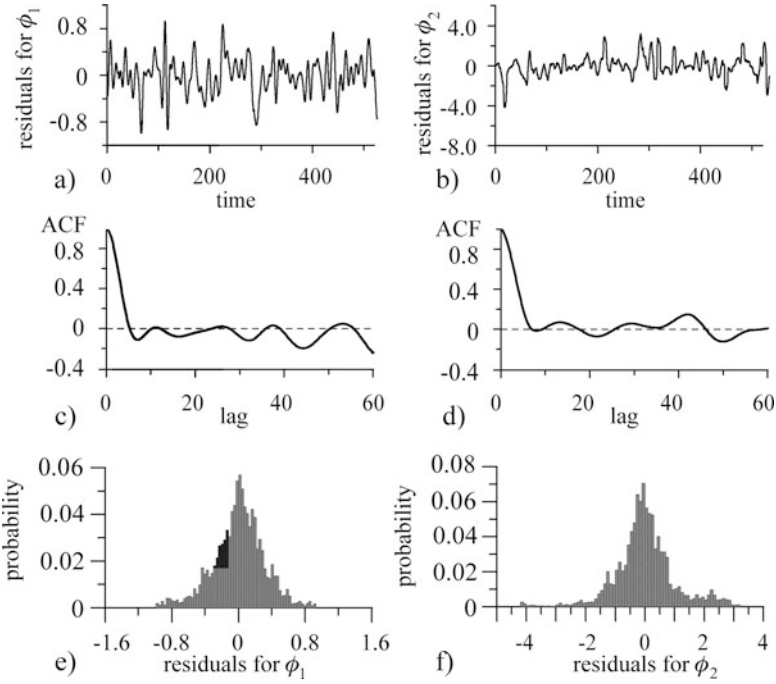

Fig. 13.20 Residual errors of the optimal phase dynamics model (13.10) for the time series of Fig. 13.18. The left column shows the residuals for the phase ϕ_1 and the right one is for the phase ϕ_2: (**a**), (**b**) the residual errors versus time; (**c**), (**d**) their autocorrelation functions; (**e**), (**f**) their histograms

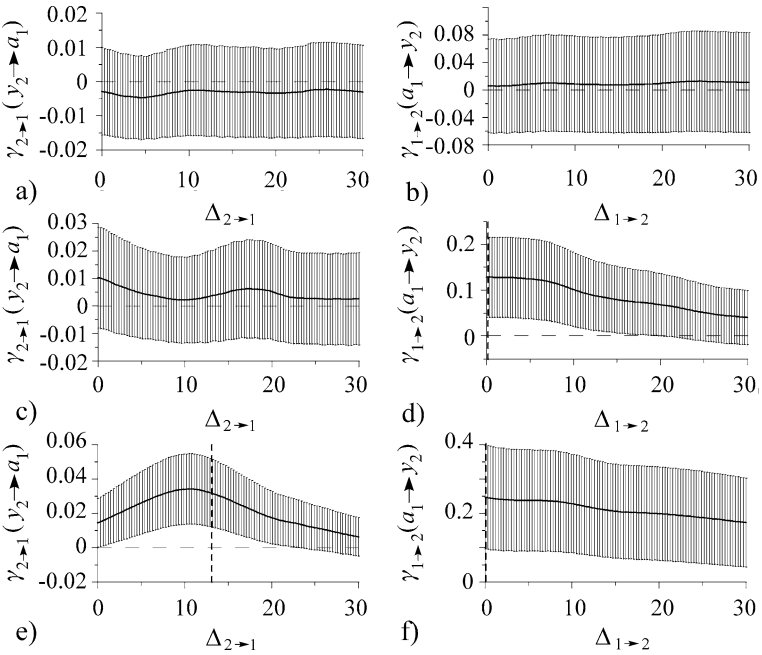

Fig. 13.21 The coupling characteristics averaged over ensembles of the time series from the system (13.11). The *error bars* indicate the averaged values of the analytic 95% confidence bands. The vertical *dashed lines* show true delay times: (**a**), (**b**) uncoupled oscillators; (**c**), (**d**) a unidirectional coupling with $k_{2\to1} = 0,\ k_{1\to2} = 0.07,\ \tau_{1\to2} = 0$; (**e**), (**f**) a bidirectional time-delayed coupling with $k_{2\to1} = 0.2,\ \tau_{2\to1} = 13.0,\ k_{1\to2} = 0.05,\ \tau_{1\to2} = 0$ (an example of a single time series for these parameters is given in Figs. 13.18, 13.19 and 13.20)

evidences that there is no false coupling detection on average. For a unidirectional "hand-to-brain" coupling ($k_{2\to1} = 0,\ k_{1\to2} = 0.07,\ \tau_{1\to2} = 0$), the unidirectional coupling pattern is observed in Fig. 13.21c, d. The experimental coupling pattern of Fig. 12.3 is qualitatively reproduced in our model (13.11) with a bidirectional time-delayed coupling, e.g., for $k_{2\to1} = 0.2,\ \tau_{2\to1} = 13.0$ (i.e. twice as large as the basic period of the oscillations), $k_{1\to2} = 0.05,\ \tau_{1\to2} = 0$, see Fig. 13.21e, f. At that, $\gamma_{2\to1}$ gets maximal for $\hat{\Delta}_{2\to1} = 9.0$, which is smaller than $\tau_{2\to1} = 13.0$ approximately by 0.6 of the basic period. For a range of true coupling coefficients and time delays, we have observed that the time delay estimate is less than the true time delay by half of the basic period on average.

Thus, with the numerical example we have qualitatively illustrated that reasonable estimates of the time delays are obtained with the phase dynamics modelling technique. Quantitatively, the time delay estimates may have an error about half a basic period and, hence, are not very accurate. Yet, we can conclude that the time delay in the brain-to-hand influence estimated from the parkinsonian tremor data is greater than the delay in the hand-to-brain direction.

To summarise, the results of the work (Smirnov et al., 2008), described above, fit to the assumption that the subcortical oscillations drive and synchronise premotor

and motor cortex which activates the contralateral muscles via the spinal cord (Brown, 2003; Rivlin-Etzion et al., 2006; Tass et al., 1998; Timmermann et al., 2003). However, the long brain-to-tremor delay indicates a more complex mechanism compared to a simple forward transmission. In contrast, the short tremor-to-brain delay fits to a direct neural transmission time of a proprioceptive feedback loop (Eichler, 2006). These results provide a new picture of the old servo loop oscillation concept, where feedback and feed-forward are acting via straight transmission lines (Stilles and Pozos, 1976). Rather, one can suggest that the synchronised subcortical oscillatory activity feeds into a multistage re-entrant processing network, most likely involving cortico-subcortical and spinal reflex loops (see also Brown, 2003; Rivlin-Etzion et al., 2006, Stilles and Pozos, 1976).

13.3 El-Niño/Southern Oscillation and Indian Monsoon

13.3.1 Object Description

Major climatic processes in Asian – Pacific region, which are of global importance, are related with the phenomena of El-Niño/Southern Oscillation (ENSO) and Indian monsoon (Solomon et al., 2007). The strongest interannual variations in the global surface temperature depend on the intensity of the ENSO phenomenon. Two-thirds of the Earth population live in the monsoon-related regions with a key role of Indian monsoon (Zhou et al., 2008). Thus, investigation of the interaction between ENSO and Indian monsoon activity is of both regional and global interest.

The presence of interdependence between these processes has been reliably detected with different techniques in many works (Kripalani and Kulkarni, 1997; 2001, Krishnamurthy and Goswami, 2000; Kumar et al., 1999; Maraun and Kurths, 2005; Sarkar et al., 2004; Solomon et al., 2007; Walker and Bliss, 1932; Yim et al., 2008; Zubair and Ropelewski, 2006). Indeed, an increase in the sea surface temperature (SST) in equatorial Pacific during El-Nino along with the corresponding change in convective processes, the Walker zonal circulation, the Hadley meridional circulation and the displacement of the intertropical convergence zone, is accompanied by considerable seasonal anomalies of temperature and precipitation in many regions. At that, there are significant variations in the correlation between characteristics of ENSO and Indian monsoon, in particular, its noticeable decrease starting from the last quarter of the XX century (Solomon et al., 2007). Along with the characterisation of an overall coupling strength provided by the coherence and synchronisation analysis, climatologists are strongly interested in a quantitative estimation of directional couplings between ENSO and Indian monsoon along with tendencies of their temporal changes.

Below, we describe estimation of the directional couplings by using the empirical AR models, i.e. the Granger causality (Sect. 12.1), which gets more and more often used in the Earth sciences (Mokhov and Smirnov, 2006, 2008; Mosedale et al., 2006; Wang et al., 2004).

13.3.2 Data Acquisition and Preliminary Processing

We have analysed monthly values of the ENSO and Indian monsoon indices for the period 1871–2006 illustrated in Fig. 13.22. Indian monsoon is characterised by variations in all-India monthly precipitation (Mooley and Parthasarathy, 1984). The corresponding data of the Indian Institute of Tropical Meteorology are available at http://climexp.knmi.nl/data/pALLIN.dat. As the ENSO index, we use SST in the area Niño-3 (5S–5N, 150W–90W) in the Pacific Ocean. We take the UK Meteorological Office GISST2.3 data for the period 1871–1996 (Rayner et al., 2003), which are available at http://paos.colorado.edu/research/wavelets/nino3data.asc, and supplement them with the data of the Climate Prediction Center obtained via Reynolds' optimal interpolation (Reynolds and Smith, 1994) for the period 1997–2006, which are available at http://www.cpc.noaa.gov/data/indices/sstoi.indices. The concatenation of the data is done in analogy with the work of Torrence and Compo presented at http://atoc.colorado.edu/research/wavelets/wavelet1.html.

Seasonal variations in both processes are clearly seen in Fig. 13.22. They are related to the common external driving, i.e. to the insolation cycle. Common exter-

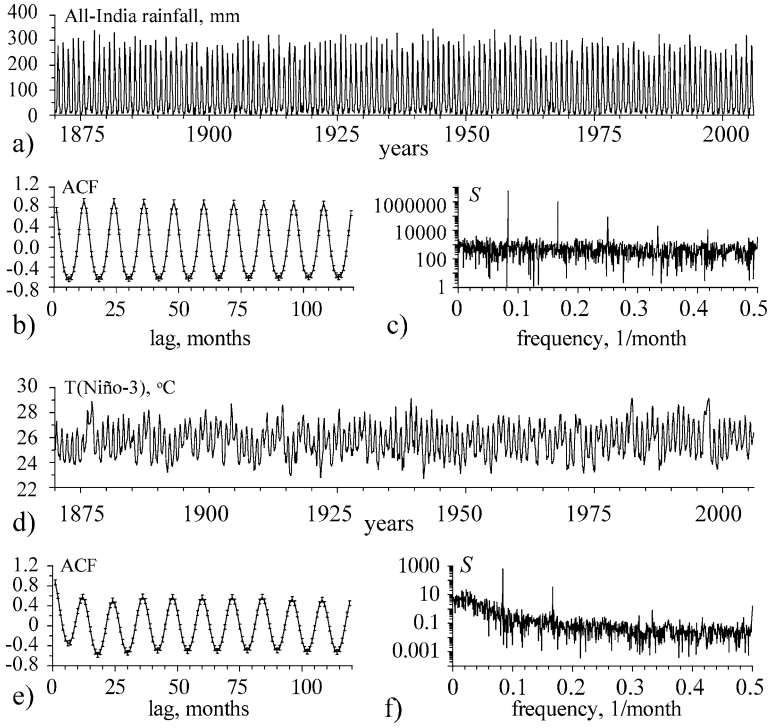

Fig. 13.22 Climatic data available and their characteristics: (**a**) an index of Indian monsoon, (**b**) its ACF estimate; the error bars show 95% confidence intervals according to Bartlett's formula (Bartlett, 1978); (**c**) its periodogram; (**d**) an ENSO index, (**e**) its ACF estimate, (**f**) its periodogram

nal driving can lead to prediction improvements (Sect. 12.1) and to erroneous conclusions about the presence of mutual influences. Therefore, we have removed the component with 12-month period and its higher harmonics from both signals. It is realised as follows. An averaged value of an observed quantity η is computed separately for each calendar month, e.g. for January. The averaging is performed over the entire interval 1871–2006. This averaged value is subtracted from all the January values of η. The values of η corresponding to each of the 12 months are processed analogously. Below, we deal only with such deseasonalised signals and denote the resulting monsoon index as $x_1(t)$ and the ENSO index as $x_2(t)$. The resulting time series are shown in Fig. 13.23a, d and their length is $N = 1632$ data points. Their power spectra and ACFs do not reveal any signs of a 12-month cycle (Fig. 13.23b, c, e, f) as desired.

The cross-correlation function for the signals $x_1(t)$ and $x_2(t)$ reaches the value of -0.22 for the 3-month time delay of the ENSO index relative to the monsoon index (Fig. 13.24). According to Bartlett's formula (Bartlett, 1978), the width of a pointwise 95% confidence band for the CCF estimate is ± 0.05. Therefore, although the absolute value of the CCF is not very large, its difference from zero at the time lags close to zero is highly statistically significant. The CCF indicates the presence of an

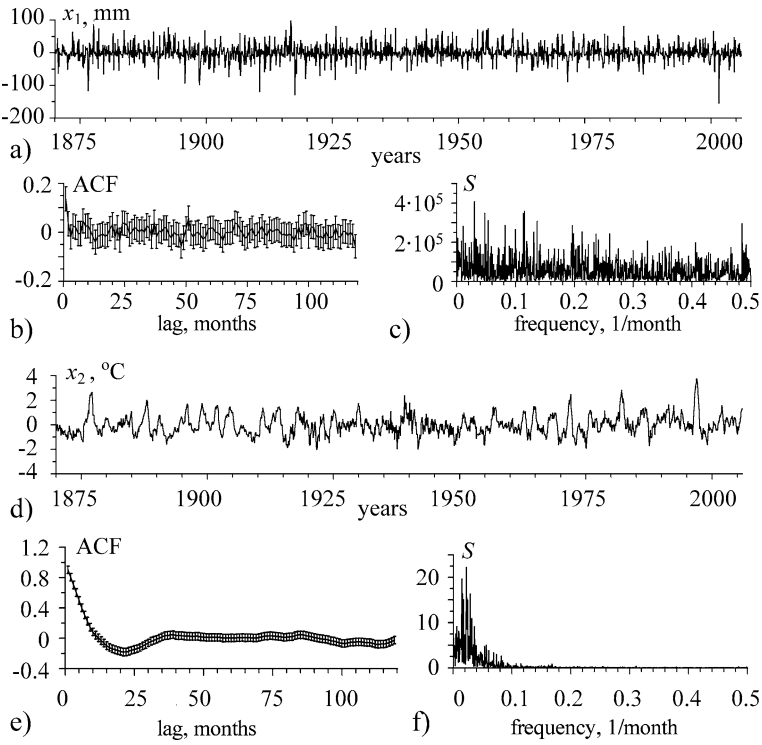

Fig. 13.23 Climatic data after the removal of the 12-month component: (**a**)–(**c**) an index of Indian monsoon with its ACF and periodogram; (**d**)–(**f**) an ENSO index with its ACF and periodogram

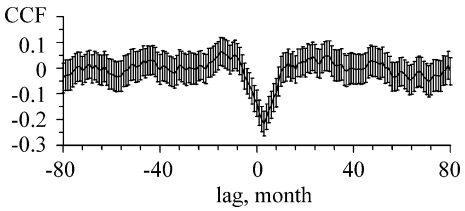

Fig. 13.24 The cross-correlation function between deseasonalised monsoon and ENSO indices

interdependence between the processes, but it does not allow to reveal whether the coupling is unidirectional (and, then, to find out its directionality) or bidirectional.

13.3.3 Selection of the Model Equation Structure

Since any a priori information about an appropriate model structure is absent, we use universal autoregressive models (Sect. 12.1) to describe the observed dynamics and reveal the character of coupling. Namely, individual (univariate) models are constructed in the form

$$\begin{aligned} x_1(t) &= f_1(x_1(t-1),\ldots,x_1(t-d_1)) + \xi_1(t), \\ x_2(t) &= f_2(x_2(t-1),\ldots,x_2(t-d_2)) + \xi_2(t), \end{aligned} \tag{13.12}$$

where f_1 and f_2 are polynomials of the orders P_1 and P_2, respectively, d_1 and d_2 are the model dimensions (orders), ξ_1 and ξ_2 are Gaussian white noises. Analogously, the joint (bivariate) model structure is

$$\begin{aligned} x_1(t) &= f_{1|2}\,(x_1(t-1),\ldots,x_1(t-d_1), x_2(t-1),\ldots, x_2(t-d_{2\to 1})) + \eta_1(t), \\ x_2(t) &= f_{2|1}\,(x_2(t-1),\ldots,x_2(t-d_2), x_1(t-1),\ldots, x_1(t-d_{1\to 2})) + \eta_2(t), \end{aligned} \tag{13.13}$$

where $f_{2|1}$ and $f_{1|2}$ are polynomials of the same orders P_1 and P_2 as for the individual models (13.12), $d_{2\to 1}$ and $d_{1\to 2}$ are the numbers of the values of the other process taken into account (they characterise inertial properties of couplings), η_1 and η_2 are Gaussian white noises.

Polynomial coefficients in the models (13.12) and (13.13) are estimated via the *ordinary least-squares technique*, i.e. via minimisation of the sums of the squared residual errors (Sect. 12.1). Since any a priori information about an appropriate model structure is absent, we try different values of d_k, $d_{j\to k}$ and P_k to find optimal ones. It is important to select the form of the non-linear functions properly. Due to relatively short time series at hand, we use low-order algebraic polynomials (Ishiguro et al., 2008; Mokhov and Smirnov, 2006) as a reasonable universal choice under the "black box" problem setting (Chap. 10).

Concretely, to select d_k, $d_{j\to k}$ and P_k, we proceed as follows. At a fixed P_k, the value of d_k is selected according to Schwarz's information criterion (see the discussion of the cost functions in Sect. 7.2.3), i.e. so as to minimise the value of

$$S_k = \frac{N}{2}\ln\hat{\sigma}_k^2 + \frac{\ln N}{2}P_k,$$

where $\hat{\sigma}_k^2$ is the minimal mean-squared prediction error of the individual AR model (13.12) at the given d_k and P_k (see the notations in Sect. 12.1). Then, we validate the univariate AR model obtained. Firstly, we check whether its residual errors are delta correlated to assure further applicability of the F-test for the coupling estimation (Sect. 12.1). Secondly, we check whether its time realisations are close to the observed time series $x_k(t)$ in a statistical sense: temporal profiles look similar; the ranges of probable values of the model and observed variables are almost the same. If all that is fulfilled, then the univariate model is regarded satisfactory, otherwise the value of d_k is increased.

Given d_k, we use Schwarz's criterion to select $d_{j\to k}$, i.e. we minimise

$$S_{j\to k} = \frac{N}{2}\ln\hat{\sigma}_{k|j}^2 + \frac{\ln N}{2}P_{k|j},$$

where $\hat{\sigma}_{k|j}^2$ is the minimal mean-squared prediction error of the bivariate AR model (13.13). However, for the purposes of coupling detection, another approach may be even more appropriate: one can select such value of $d_{j\to k}$, which maximises $\mathrm{PI}_{j\to k} = \hat{\sigma}_k^2 - \hat{\sigma}_{k|j}^2$ or corresponds to the value of $\mathrm{PI}_{j\to k}$, which exceeds zero at the smallest significance level p. We use the latter approach as well and compare the results of both approaches. An obtained bivariate AR model is validated in the same way as the univariate models.

Different values of P_k are tried. The above analysis, including the selection of d_k and $d_{j\to k}$, is performed for each P_k. The most appropriate value of P_k is selected both according to Schwarz's criterion and to the most significant $\mathrm{PI}_{j\to k}$ and the results are compared. The trial values of d_k, $d_{j\to k}$ and P_k are varied within such a range that the number of coefficients in any fitted AR model remains much less than the time series length N, namely the number of model coefficients does not exceed $\sqrt{N}$, i.e. approximately 40 in our case.

13.3.4 Model Fitting, Validation and Usage

Firstly, we fit models and estimate couplings for the entire period 1871–2006. Secondly, the analysis is done in moving windows of length ranging from 10 to 100 years to get time-resolved coupling characteristics.

13.3.4.1 Univariate models

The number of coefficients in the linear models is equal to $P_k = d_k + 1$ so that d_k can be increased up to 39 when a model is fitted to the entire period 1871–2006. For the quadratic models, we get

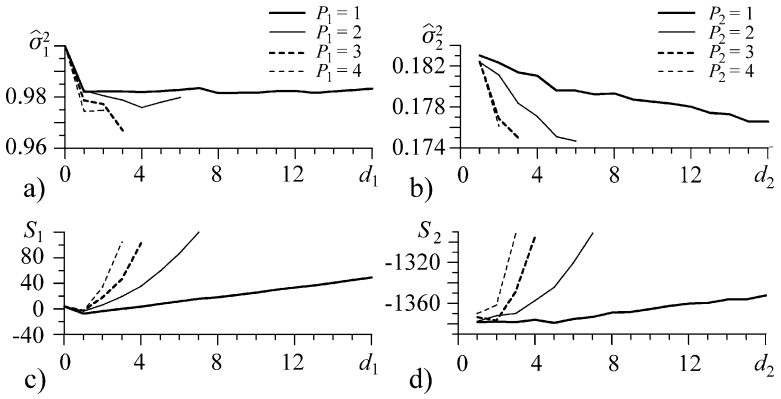

Fig. 13.25 Mean-squared prediction errors (*first row*) and Schwarz's criterion (*second row*) for the individual AR models of the Indian monsoon index (*left column*) and the ENSO index (*right column*)

$$P_k = \frac{(d_k + 1)(d_k + 2)}{2}$$

so that d_k may not exceed 7. It should be $d_k \leq 4$ for $P_k = 3$, $d_k \leq 3$ for $P_k = 4$, etc.

For the monsoon index, an optimal model is achieved at $d_1 = 1$ for any P_1 (Fig. 13.25a, c). Schwarz's criterion takes the smallest values for the linear models. Thus, an optimal model is linear with $d_1 = 1$. It gives a prediction error with the variance $\hat{\sigma}_1^2/\mathrm{var}[x_1] = 0.98$, where $\mathrm{var}[x_1]$ is the sample variance of x_1. The model explains only 2% of $\mathrm{var}[x_1]$.

For the ENSO index, an optimal model dimension is $d_2 = 1$ at $P_2 = 2, 4$ and $d_2 = 2$ at $P_2 = 3$, but the best model is linear with $d_2 = 5$ (Fig. 13.25b, d). The normalised variance of its prediction error is $\hat{\sigma}_2^2/\mathrm{var}[x_2] = 0.18$.

The obtained individual models appear valid: the residual errors of the optimal models (Fig. 13.26a, d) for both processes are delta correlated (Fig. 13.26b, e) and exhibit distributions with quickly decreasing tails (Fig. 13.26c, f); model time realisations are statistically close to the observed data (the plots are not shown, since they are similar to those for a bivariate model presented below).

13.3.4.2 ENSO-to-Monsoon Driving

To construct bivariate models for the monsoon index, we use $d_1 = 1$ at different values of P_1 based on the results shown in Fig. 13.25c. The value of $d_{2\to1} = 1$ appears optimal at $P_1 = 1$ and 3 (Fig. 13.27a). The linear model gives the smallest value of Schwarz' criterion. However, the model with $P_1 = 3$ gives greater and the most statistically significant prediction improvement (Fig. 13.27c, e). This is a sign of non-linearity in the ENSO-to-monsoon influence, which would be ignored if the linear model were used to estimate the coupling. To avoid such a negligence, we regard the model with $P_1 = 3$ as optimal. Its prediction improvement

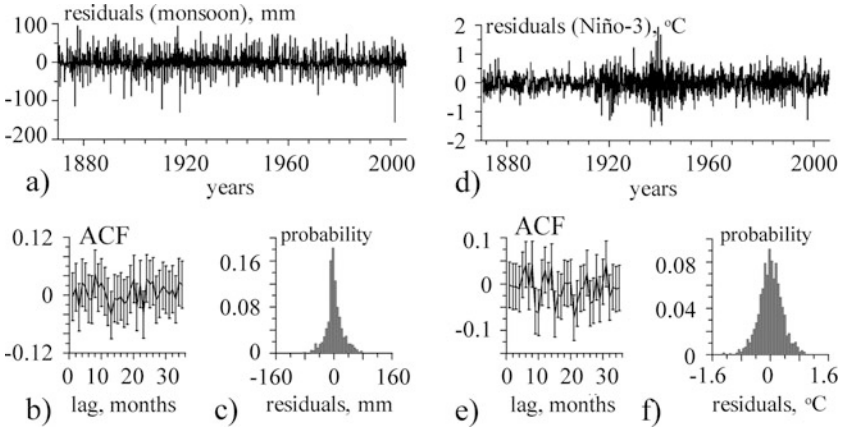

Fig. 13.26 Residual errors of the optimal individual models (13.12) with ACFs and histograms: (**a**)–(**c**) for the Indian monsoon index; (**d**)–(**f**) for the ENSO index

is $\mathrm{PI}_{2\to1}/\hat{\sigma}_1^2 = 0.028$, i.e. it equals only 2.8% of the variance of all factors, which remain unexplained by the univariate model. Yet, the ENSO-to-monsoon influence is detected with high confidence ($p < 10^{-8}$).

The optimality of the value of $d_{2\to1} = 1$ means "inertialless" ENSO-to-monsoon influence. The model reads as

$$x_1(t) = a_{1,1}x_1(t-1) + b_{1,1}x_2(t-1) + c_{1,1}x_1^2(t-1)x_2(t-1) + c_{1,2}x_2^3(t-1) + \eta_1(t), \tag{13.14}$$

where $\sigma_{\eta_1}^2 = 5.84 \times 10^2\,\mathrm{mm}^2$ and estimates of the coefficients and their standard deviations (see Sect. 7.4.1 and Seber, 1977) are the following: $a_{1,1} = 0.071 \pm 0.035$, $b_{1,1} = -4.65 \pm 1.11\,\mathrm{mm\,K^{-1}}$, $c_{1,1} = (-3.53 \pm 0.76) \cdot 10^{-3}\,\mathrm{mm^{-1}\,K^{-1}}$ and $c_{1,2} = 1.53 \pm 0.38\,\mathrm{mm\,K^{-3}}$. We have shown only the terms whose coefficients differ from zero at least at the pointwise significance level of 0.05, i.e. the absolute value of a coefficient is at least twice as big as its standard deviation. The linear coupling coefficient $b_{1,1}$ is negative, which corresponds to the above-mentioned negative correlation between the signals x_1 and x_2.

13.3.4.3 Monsoon-to-ENSO Driving

A bivariate model for the ENSO index is optimal at $P_2 = 1$ and $d_{1\to2} = 3$ (Fig. 13.27b). It corresponds to the most significant prediction improvement $\mathrm{PI}_{1\to2}/\hat{\sigma}_2^2 = 0.024$ exceeding zero at the significance level of $p < 10^{-8}$ (Fig. 13.27d, f). The model reads as

$$x_2(t) = a_{2,1}x_2(t-1) + a_{2,5}x_2(t-5) + b_{2,1}x_1(t-1) + b_{2,2}x_1(t-2) + b_{2,3}x_1(t-3) + \eta_2(t), \tag{13.15}$$

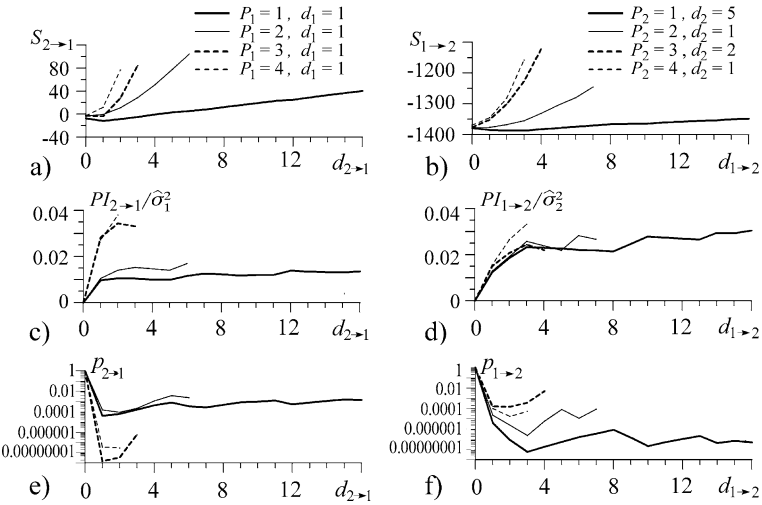

Fig. 13.27 Fitting the bivariate models to the monsoon (the *left column*) and ENSO (the *right column*) data: Schwarz's criterion (*first row*), the prediction improvement (*second row*) and the significance level (*third row*)

where $\sigma_{\eta_2}^2 = 0.11\,\mathrm{K}^2$, $a_{2,1} = 0.92 \pm 0.025$, $a_{2,5} = -0.083 \pm 0.025$, $b_{2,1} = (-1.44 \pm 0.34) \times 10^{-3}\,\mathrm{mm}^{-1}\,\mathrm{K}$, $b_{2,2} = (-1.04 \pm 0.35) \times 10^{-3}\,\mathrm{mm}^{-1}\,\mathrm{K}$ and $b_{2,3} = (-1.01 \pm 0.35) \times 10^{-3}\,\mathrm{mm}^{-1}\,\mathrm{K}$. The monsoon-to-ENSO influence is inertial, since the optimal value of $d_{1\to2} > 1$. Namely, the behaviour of the ENSO index depends on the values of the monsoon index for three previous months. The coupling coefficients $b_{2,1}, b_{2,2}, b_{2,3}$ are negative and also correspond to the observed anti-correlation between x_1 and x_2. All the three coupling coefficients are almost identical, i.e. the total contribution of the monsoon index to equation (13.15) $(b_{2,1}x_1(t-1) + b_{2,2}x_1(t-2) + b_{2,3}x_1(t-3))$ is approximately proportional to its average value over 3 months. No signs of non-linearity of the monsoon-to-ENSO influence are detected.

13.3.4.4 Validation of the Bivariate Model

ACFs and histograms of the residual errors for the bivariate models (13.14) and (13.15) are very similar to those for the individual models in Fig. 13.26; they exhibit delta correlatedness and quickly decreasing tails (not shown). The correlation coefficient between the residual errors for the monsoon and ENSO indices is 0.02 ± 0.05, i.e. equals zero within the estimation error. Thus, the noises η_1 and η_2 are considered independent when realisations of the bivariate model (13.14) and (13.15) are simulated. Time realisations of this optimal model with $P_1 = 3$, $d_1 = 1$, $d_{2\to1} = 1$, $P_2 = 1$, $d_2 = 5$, $d_{1\to2} = 3$ look similar to the observed time series (Fig. 13.28a,c). For a quantitative comparison, an ensemble of model realisations at the same initial conditions is generated and 95% intervals of the distributions

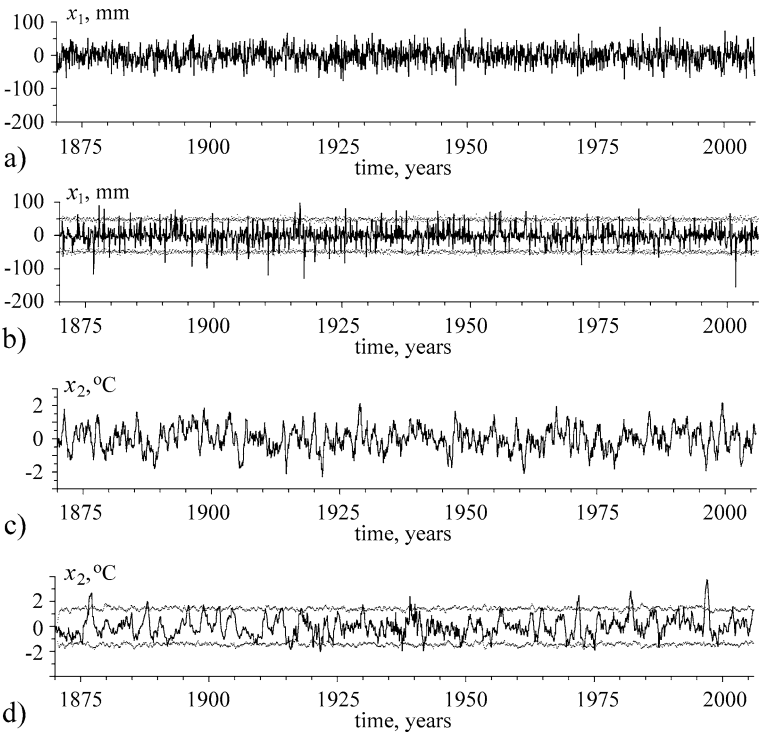

Fig. 13.28 Behaviour of the optimal AR model (13.14) and (13.15): (**a**), (**c**) model time realisations corresponding to the monsoon index and the ENSO index, respectively; (**b**), (**d**) 95% intervals of the model variables (*dotted lines*) and the observed data (*solid lines*), respectively

of the model variables are determined. It appears that 95% of the observed values of the ENSO and monsoon indices fall within those intervals (Fig. 13.28b,d), which confirms validity of the model.

13.3.4.5 Coupling Analysis in Moving Window

Finally, let us consider temporal variations in the coupling characteristics by using the moving window analysis, i.e. the intervals $[T - W, T]$, where W is the window length and T is a coordinate of the window endpoint (in years). At a fixed value of W (which is systematically changed from 10 years to 100 years with a step of 10 years), the Granger causality estimates are calculated for T ranging from $1871 + W$ till 2006.

To assess significance levels of the conclusions about the coupling present under the moving-window scenario, a multiple test correction (Lehmann, 1986) must be applied. Namely, according to the above procedure, one gets the estimates of the prediction improvement $\mathrm{PI}_{j\to k}$ and the corresponding significance level p for each time window. This is the so-called pointwise significance level, i.e. a probability of

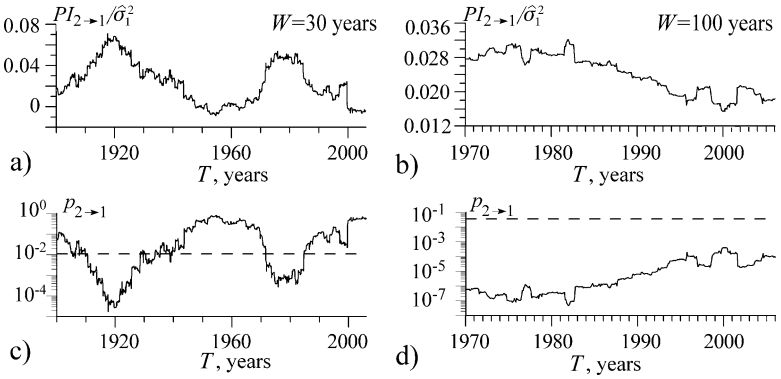

Fig. 13.29 Estimates of the ENSO-to-monsoon influence in a moving window $[T-W, T]$ versus the coordinate of the window endpoint T: (**a**), (**b**) prediction improvements; (**c**), (**d**) pointwise significance levels. Different panels show the results for the two different window lengths of 30 and 100 years. The *dashed lines* show the critical values p_c of the pointwise significance level corresponding to the resulting significance level of $p = 0.05$ (see the text)

a random erroneous conclusion for a single time window considered separately. The probability of a false positive conclusion at the pointwise level p for at least one of M non-overlapping time windows may reach the value of $p \cdot M$, because probability of a union of independent events is approximately equal to the sum of their individual probabilities (if the resulting value $p \cdot M$ is still much less than unity). Thus, one can establish the presence of coupling for a particular time window among M non-overlapping windows at a "true" significance level p if the pointwise significance level for this window equals p/M, where the multiplier $1/M$ is called the Bonferroni correction. The dashed lines in Figs. 13.29 and 13.30 show such a

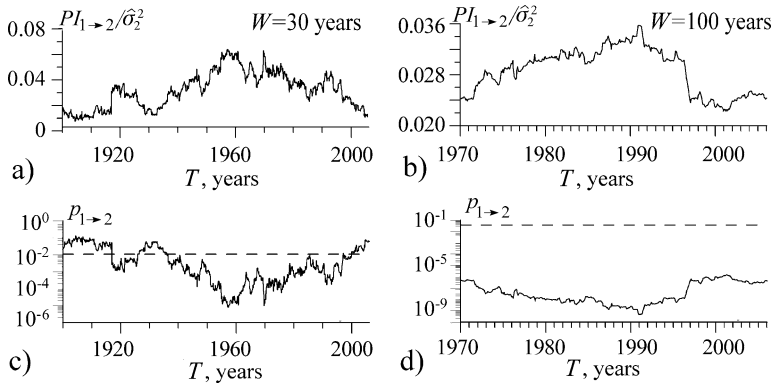

Fig. 13.30 Estimates of the monsoon-to-ENSO influence in a moving window $[T-W, T]$ versus the coordinate of the window endpoint T: (**a**), (**b**) prediction improvements; (**c**), (**d**) pointwise significance levels. Different panels show the results for the two different window lengths of 30 and 100 years. The *dashed lines* show the critical values p_c of the pointwise significance level corresponding to the resulting significance level of $p = 0.05$ (see the text)

threshold value of $p_c = 0.05/(N/W)$, where N/W estimates the number of non-overlapping windows; if the pointwise significance level p for any time window gets less than p_c, we infer coupling presence for this window at the resulting significance level less than 0.05.

Estimates of the ENSO-to-monsoon driving for the optimal non-linear model with the parameters $d_1 = d_{2\to 1} = 1$, $P_1 = 3$ are presented in Fig. 13.29 for the window lengths of 30 years (Fig. 13.29a, c) and 100 years (Fig. 13.29b, d). The 100-year windows give highly significant results for any T. A long-term tendency consists of a weak rise of the ENSO-to-monsoon coupling strength at the beginning of the investigated period, reaching a maximum, and a subsequent decrease. The duration of the decrease period is longer than that of the rise period. When the time window length is decreased, the temporal resolution enhances at the expense of the significance of the results. Thus, the 30-year windows reveal coupling for $1910 \le T \le 1930$ and $1975 \le T \le 1985$, i.e. over the intervals 1880–1930 and 1945–1985. For shorter moving windows, the non-linear model gets relatively too "big" and gives less significant results. In total, the ENSO-to-monsoon driving is relatively weak before 1880, during the period 1930–1945 and after 1985.

One can see statistically significant influence of the monsoon on ENSO in a 100-year moving window for any T (Fig. 13.30). A long-term tendency is the same as for the ENSO-to-monsoon driving, but the monsoon-to-ENSO coupling strength starts to decrease later; a maximum of its temporal profile is closer to the year of 2006. A significant monsoon-to-ENSO influence in a 30-year window is observed for $1917 \le T \le 1927$ and, especially, for $1935 \le T \le 2000$. With a 20-year moving window, a significant influence is detected only over the interval 1930–1960; with a 10-year moving window, it is not detected at all (the plots are not shown). In total, the monsoon-to-ENSO influence is not seen only before 1890 and it is the most essential during the period 1930–1950.

Thus, the intervals of the strongest ENSO-to-monsoon and monsoon-to-ENSO influences do not coincide in time but follow each other. The coupling between both processes is approximately symmetric "in strength": the normalised prediction improvement is about 2–3% for the entire interval 1871–2006 and reaches about 7% in a 30-year moving window for both directions.

We note that in Maraun and Kurths (2005) the authors found intervals of 1:1 synchronisation between both signals, i.e. the intervals when the phase difference $\phi_1 - \phi_2$ is approximately constant. These are the intervals 1886–1908 and 1964–1980, which correspond to the strong ENSO-to-monsoon influence detected by the Granger causality. Next, the intervals of 1:2 synchronisation (when the difference $\phi_1 - 2\phi_2$ is approximately constant) appear during 1908–1921 (corresponds to a predominant monsoon-to-ENSO driving detected with the Granger causality), 1935–1943 (the strongest monsoon-to-ENSO driving and no significant ENSO-to-monsoon driving) and 1981–1991 (a predominant monsoon-to-ENSO driving). Thus, the 1:1 synchronisation coincides with the intervals of a stronger ENSO-to-monsoon influence, while the 1:2 synchronisation to a predominant monsoon-to-ENSO influence.

13.4 Conclusions

The investigation of coupling between the climatic processes considered here represents a black-box problem. With the universal model structure (polynomial AR models), we have obtained valid models and used them to characterise directional couplings between ENSO and Indian monsoon. The results complement previous knowledge of anti-correlation between these processes (Walker and Bliss, 1932) and their phase synchrony intervals (Maraun and Kurths, 2005). Namely, the empirical modelling has revealed bidirectional coupling between ENSO and Indian monsoon with high confidence. The ENSO-to-monsoon influence appears inertialless and non-linear. The monsoon-to-ENSO influence is linear and inertial; the values of the monsoon index for three months affect the future behaviour of the ENSO index. However, in some sense the coupling is symmetric; prediction improvement is about 2–3% in both directions. The moving window analysis has revealed an alternating character of the coupling. The monsoon-to-ENSO coupling strength rises since the end of the nineteenth century till approximately the period of 1930–1950, when it is maximal. This influence weakens in the last decade of the twentieth century. The opposite influence is strongest during the period of 1890–1920. It is also noticeable in 1950–1980 and not detected in 1920–1950 and after 1980.

To summarise, the three examples considered in Chap. 13 illustrate an empirical modelling procedure under three different settings: complete a priori information about a model structure, partial information and no information. The first setting takes place for the laboratory electronic systems, which is typical since laboratory experiments can be devised so as to control many properties of the objects under study. The second setting corresponds to a physiological problem, where partial information about an appropriate model structure is available due to specific properties (considerable regularity) of the observed signals. The third example of no specific knowledge about a model structure is taken from climatology. Estimates of couplings between the investigated processes provided by the empirical modelling can be regarded as most "valuable" in the latter case, where the results seem to be obtained practically "from nothing". However, under all the three settings, empirical modelling allows to get useful information such as validation of the physical ideas behind model equations and quantitative characterisation of individual dynamics and interactions.

References

Bartlett, M.S.: Stochastic Processes. Cambridge University Press: Cambridge (1978)

Benabid, A.L., Pollak, P., Louveau, A., Henry, S., de Rougemont, J. Combined (thalamotomy and stimulation) stereotactic surgery of the VIM thalamic nucleus for bilateral Parkinson's disease. Appl. Neurophysiol. **50**, 344–346 (1987)

Bezruchko, B.P., Ponomarenko, V.I., Prokhorov, M.D., Smirnov, D.A., Tass, P.A.: Modeling nonlinear oscillatory systems and diagnostics of coupling between them using chaotic time series analysis: applications in neurophysiology. Physics – Uspekhi. **51**, 304–310 (2008)

Brown, P.: Oscillatory nature of human basal ganglia activity: relationship to the pathophysiology of Parkinson's disease. Mov. Disord. **18**, 357–363 (2003)
Deuschl, G., Krack, P., Lauk, M., Timmer, J.: Clinical neurophysiology of tremor. J. Clin. Neurophysiol. **13**, 110–121 (1996)
Dietz, V.: Spinal cord pattern generators for locomotion. Clin. Neurophysiol. **114**, 1379–1389 (2003)
Dmitriev, A.S., Kislov, V.Ya. Stochastic Oscillations in Radiophysics and Electronics. Nauka, Moscow, (in Russian) (1989)
Dmitriev, A.S., Panas, A.I., Starkov, S.O.: Ring oscillating systems and their application to the synthesis of chaos generators. Int. J. Bifurc. Chaos. **6**, 851–865 (1996)
Eichler, M.: Graphical modelling of dynamic relationships in multivariate time series. In: Winterhalder, M., Schelter, B., Timmer, J. (eds) Handbook of Time Series Analysis, pp. 335–367. Wiley-VCH, Berlin (2006)
Ishiguro, K., Otsu, N., Lungarella, M., Kuniyoshi, Y.: Detecting direction of causal interactions between dynamically coupled signals. Phys. Rev. E. **77**, 026216 (2008)
Kripalani, R.H., Kulkarni, A.: Monsoon rainfall variations and teleconnections over South and East Asia. Int. J. Climatol. **21**, 603–616 (2001)
Kripalani, R.H., Kulkarni, A.: Rainfall variability over Southeast Asia: Connections with Indian monsoon and ENSO extremes: New perspectives. Int. J. Climatol. **17**, 1155–1168 (1997)
Krishnamurthy, V., Goswami, B.N.: Indian monsoon-ENSO relationship on interdecadal timescale. J. Climate. **13**, 579–595 (2000)
Kuramoto, Y.: Chemical Oscillations, Waves and Turbulence. Springer, Berlin (1984)
Lehmann, E.: Testing Statistical Hypothesis. Springer, Berlin (1986)
Lenz, F.A., Kwan, H.C., Martin, R.L., Tasker, R.R., Dostrovsky, J.O., Lenz, Y.E.: Single unit analysis of the human ventral thalamic nuclear group. Tremor related activity in functionally identified cells. Brain. **117**, 531–543 (1994)
Llinas, R., Jahnsen, H.: Electrophysiology of mammalian thalamic neurones in vitro. Nature. **297**, 406–408 (1982)
Maraun, D., Kurths, J.: Epochs of phase coherence between El Nino/Southern Oscillation and Indian monsoon. Geophys. Res. Lett. **32**, L15709 (2005)
Mokhov, I.I., Smirnov, D.A.: Diagnostics of a cause – effect relation between solar activity and the earth's global surface temperature. Izvestiya, Atmos. Oceanic Phys. **44**, 263–272 (2008)
Mokhov, I.I., Smirnov, D.A.: El Nino Southern Oscillation drives North Atlantic Oscillation as revealed with nonlinear techniques from climatic indices. Geophys. Res. Lett. **33**, L0378 (2006)
Mooley, D.A., Parthasarathy, B.: Fluctuations in all-India summer monsoon rainfall during 1871–1978. Clim. Change. **6**, 287–301 (1984)
Mosedale, T.J., Stephenson, D.B., Collins, M., Mills, T.C.: Granger causality of coupled climate processes: ocean feedback on the North Atlantic Oscillation. J. Climate. **19**, 1182–1194 (2006)
Pare, D., Curro'Dossi, R., Steriade, M.: Neuronal basis of the parkinsonian resting tremor. Neuroscience. **217**, 217–226 (1990)
Pikovsky, A.S., Rosenblum, M.G., Kurths, J.: Phase synchronization in regular and chaotic systems. Int. J. Bif. Chaos. **10**, 2291–2305 (2000)
Pikovsky, A.S., Rosenblum, M.G., Kurths, J.: Synchronisation. A Universal Concept in Nonlinear Sciences. Cambridge: Cambridge University Press (2001)
Ponomarenko, V.I., Smirnov, D.A., Bodrov, M.B., Bezruchko, B.P.: Global reconstruction from time series in application to determination of coupling direction. In: Gulyaev, Yu.V., Sinitsyn, N.I., Anikin, V.M. Voprosy prikladnoy fiziki (Question of Applied Physics). Inter-University Scientific Transactions. Issue 11, pp. 192–200. College (2004)
Rayner, N.A., Parker, D.E., Horton, E.B., Folland, C.K., Alexander, L.V., Rowel, D.P., Kent, E.C., Kaplan, A.: Global analyses of sea surface temperature, sea ice, and night marine air temperature since the late nineteenth century. J. Geophys. Res. **108**(D14). doi:10.1029/2002JD002670 (2003)
Reynolds, R.W., Smith, T.M.: Improved global sea surface temperature analyses. J. Climate. **7**, 929–948 (1994)

Rivlin-Etzion, M., Marmor, O., Heimer, G., Raz, A., Nini, A., Bergman, H.: Basal ganglia oscillations and pathophysiology of movement disorders. Curr. Opin. Neurobiol. **16**, 629–637 (2006)

Rosenblum, M.G., Pikovsky, A.S., Kurths, J., Schaefer, C., Tass, P.A.: Phase synchronization: from theory to data analysis. In: Moss, F., Gielen, S. (eds.) Neuro-Informatics. Handbook of Biological Physics, vol. 4, pp. 279–321.Elsevier Science, New York (2001)

Sarkar, S., Singh, R.P., Kafatos, M.: Further evidences for the weakening relationship of Indian rainfall and ENSO over India. Geophys. Res. Lett. **31**, L13209. doi:10.1029/2004GL020259 (2004)

Seber, G.A.F.: Linear Regression Analysis. Wiley, New York (1977)

Smirnov, D., Barnikol, U.B., Barnikol, T.T., Bezruchko, B.P., Hauptmann, C., Buehrle, C., Maarouf, M., Sturm, V., Freund, H.-J., Tass, P.A.: The generation of Parkinsonian tremor as revealed by directional coupling analysis. Europhys. Lett. **83**, 20003 (2008)

Smirnov, D., Schelter, B., Winterhalder, M., Timmer, J.: Revealing direction of coupling between neuronal oscillators from time series: Phase dynamics modeling versus partial directed coherence. Chaos. **17**, 013111 (2007)

Smirnov, D.A., Andrzejak, R.G.: Detection of weak directional coupling: phase dynamics approach versus state space approach. Phys. Rev. E. **71**, 036207 (2005)

Smirnov, D.A., Bezruchko, B.P.: Estimation of interaction strength and direction from short and noisy time series. Phys. Rev. E. **68**, 046209 (2003)

Solomon, S., Qin, D., Manning, M., Marquis, M., Averyt, K., Tignor, M.M.B., LeRoy Miller, H., Chen, Z. (eds.): Climate Change 2007: The Physical Science Basis. Cambridge University Press: Cambridge (2007)

Stilles, R., Pozos, R. A mechanical-reflex oscillator hypothesis for parkinsonian hand tremor. J. Appl. Physiol. **40**, 990–998 (1976)

Tass, P.A.: Phase Resetting in Medicine and Biology. Springer, Berlin (1999)

Timmer, J., Haeussler, S., Lauk, M., Luecking, C.H.: Pathological tremors: deterministic chaos or nonlinear stochastic oscillators?. Chaos. 10, 278–288 (2000)

Timmermann, L., Gross, J., Dirks, M., Volkmann, J., Freund, H.J., Schnitzler, A.: The cerebral oscillatory network of parkinsonian resting tremor. Brain. **126**, 199–212 (2003)

Treuer, H., Klein, D., Maarouf, M., Lehrke, R., Voges, J., Sturm, V.: Accuracy and conformity of stereotactically guided interstitial brain tumour therapy using I-125 see. Radiother. Oncol. **77**, 202–209 (2005)

Walker, G.T., Bliss, E.W.: World weather V. Mem. R. Meteorol. Soc. **4**, 3–84 (1932)

Wang, W., Anderson, B.T., Kaufmann, R.K., Myneni, R.B. The relation between the North Atlantic Oscillation and SSTs in North Atlantic basin. J. Climate. **17**, 4752–4759 (2004)

Yim, S.-Y., Jhun, J.-G., Yeh, S.-W.: Decadal change in the relationship between east Asian – western North Pacific summer monsoons and ENSO in the mid-1990s. Geophys. Res. Lett. **35**, L20711, doi:10.1029/2008GL035751 (2008)

Zhou, T., Zhang, L., Li, H.: Changes in global land monsoon area and total rainfall accumulation over the last half century. Geophys. Res. Lett. **35**, L16707, doi:10.1029/2008GL034881 (2008)

Zimmermann, R., Deuschl, G., Hornig, A., Schulte-Munting, J., Fuchs, G., Lucking, C.H.: Tremors in Parkinson's disease: symptom analysis and rating. Clinical Neuropharmacology. 17, 303–314 (1994)

Zubair, L., Ropelewski, C.F.: The strengthening relationship between ENSO and Northeast Monsoon rainfall over Sri Lanka and Southern India. J. Climate. **19**, 1667–1575 (2006)